CENTRO DE INVESTIGACIONES
EN OPTICA, A.C.

"DESIGN OF STABLE ORGANIC SOLAR CELLS AND PEROVSKITE SOLAR CELLS USING ADHESIVES AS ENCAPSULANTS"

Thesis to obtain the degree of Master of Science (Optics)

Author: **Amisi Austine Odiwuor**

Thesis Advisor: *Dr. José-Luis Maldonado-Rivera*

León · Guanajuato · Mexico
***December* 2021**

Abstract

Organic solar cells (OSCs) have recently been one of the promising photovoltaic (PV) technologies with numerous advantages, including reasonable power conversion efficiencies (PCEs), bandgap tunability, easy processability, low cost, and flexibility. On the other hand, perovskite solar cells (PSCs) have surprisingly emerged as highly efficient solar cells due to their unprecedented rise in PCE within the last decade. Nonetheless, extrinsic instability due to moisture and oxygen remains one of the serious problems preventing the commercialization of these devices. Encapsulation has been suggested as one of the most attractive techniques to enhance external stability. Despite their differences in terms of charge generation, OSCs and PSCs share similar materials processing, therefore, standard strategies have been developed for both of them. Herein, we aimed to design stable OSCs and PSCs using three encapsulation materials, namely Norland optical adhesive 65 (NOA 65), NOA 71, and Ossila encapsulation epoxy (OEE). The PV parameters, such as PCE, short-circuit current density (Jsc), open-circuit voltage (Voc), and fill factor (FF), were monitored for 20 days after encapsulation. Our results reveal the effect of using encapsulants on device stability. OEE had the highest performance retention of 93% and 86% in OSC and PSC, respectively, and was attributed to the trade-offs between a combination of indicators, especially water vapor transmission rate (WVTR), oxygen transmission rate (OTR), adhesion, optical performance, and refractive index. NOA 71 was second, retaining 91% and 80%, in OSC and PSC, respectively, while NOA 65 came third, retaining 87% and 78% in OSC and PSC, respectively. However, the OEE's higher cost may potentially increase the overall device production costs. Therefore, future studies could assess the economics and

include more encapsulation materials to conclusively identify the adhesive(s) that optimizes both device cell efficiency, durability, and cost.

Acknowledgments

This research work would not be possible without CONACyT's (Mexico) grant and financial support through Laboratorio Nacional de Materiales Grafénicos (LNMG). I also acknowledge Centro de Investigaciones en Óptica (CIO) and the community in general for their invaluable resources, conducive learning environment, and support necessary to carry out my thesis project.

I am also especially grateful to my thesis advisor, Dr. José-Luis Maldonado-Rivera, who has been instrumental in supervising and providing me with extensive professional and personal guidance. As my director, the feedback, suggestions, and patience he demonstrated were unimaginable.

I would also like to thank the members of my evaluation committee, Dr. Norberto Arzate Plata and Dr. Marco Antonio Meneses Nava, for taking their time to seek clarifications, comment, and evaluate me with the eventuality to attain my MSc. Degree.

I am forever indebted to everyone at the Research Group of Optical Properties of Materials (GPOM) with whom I had the pleasure to work alongside during this project. I wish to thank Dr. Wilson Bernal, Martin Olmos, and colleague researchers for their technical support, particularly in situations where I was technically challenged. I also acknowledge both Dr. Ma. Elena Nicho and Dr. Marisol Guizado from UAEMor for providing the P3HT polymer that was instrumental in organic cell fabrication.

In pursuing this project, no one has been more important to me than my family members. I would like to appreciate my stepmother, brothers, and sisters for showing me guidance and love as I embarked on this research. Most importantly, I wish to thank my loving and

supportive wife, Meroline Augo, and my wonderful daughter, Best Jemimah, for their interminable inspiration.

Contents

List of Figures

List of Tables

1. Introduction

1.1. Sustainable energy as a challenge

In the past few decades, innumerable challenges have confronted the world, and the need to address the ever-increasing global energy consumption and demand has been at the forefront, with forecasts indicating that the demand will grow by nearly 50% by 2050 [1, 2]. The growing population coupled with increased energy access and dramatic economic development of the emerging and developing countries around the world will drive this demand. Primarily, this will be accelerated by the rapid growth in device sophistication and quality that would lead to an extremely high average consumption per device in the years to come.

In addition, fossil fuels, including natural gas and oil, whose reserves have been reported to considerably decline by the 2040s, still dominate the vast majority of today's energy supply and provide ~80% of the world's energy consumption [3]. Overcoming our dependence on fossil fuels has been speculated to be a great obstacle [4]. As shown in Figure 1, the global warming threat caused by carbon emissions from sources like coal and oil is no longer refutable. Its impacts are rife in most countries. For instance, in Mexico, global warming is anticipated to have widespread effects on the country, with considerable temperature increases and precipitation reductions [5]. This will negatively impact its biodiversity, citizens, and economy [5]. Similar situations have been constantly witnessed in the rest of the world, such as the UK where temperatures have constantly soared above 30 °C, Portugal where higher than normal temperatures (40 °C) have been recorded, as well as the USA and Greece where wildfires have continually occurred. Although nuclear energy

was previously suggested as the alternative, recent works have shown nuclear power plants are vulnerable when it comes to radioactive waste management and safety [4].

Scientists have undoubtedly established that the recent prolonged extreme weather changes, such as increases in the average ocean and air temperatures, permeating melting of ice and snow and rising sea levels, as well as observed temperature increases from the mid-20th century, are as a result of climate change caused by human activities like fossil fuel burning [6]. The earth's warming is already depicting some of the quantifiable effects, and in the future, we can only anticipate more costly and wide-ranging impacts. Indeed, persistent and sustained greenhouse gas emissions at or beyond the present levels would further increase global temperatures and cause numerous other climatic changes during this century [6]. To combat these looming adversities, mounting evidence focused on climate change and carbon emission has emphasized the need to urgently transform our current energy sources to renewable alternatives and other more environment-friendly sources. Accordingly, harnessing and maximizing clean energy production using renewable energy sources, namely solar, biomass, geothermal, hydro, wind, and tidal waves, has been strongly suggested to be promising in addressing both the increasing energy demand for the growing population and today's climate change problems. Despite the potential of renewable energy resources, their current total global share is about 26%, with an expected share of approximately 40% by 2040 [7]. From this prediction, solar energy has been reported to play an integral part.

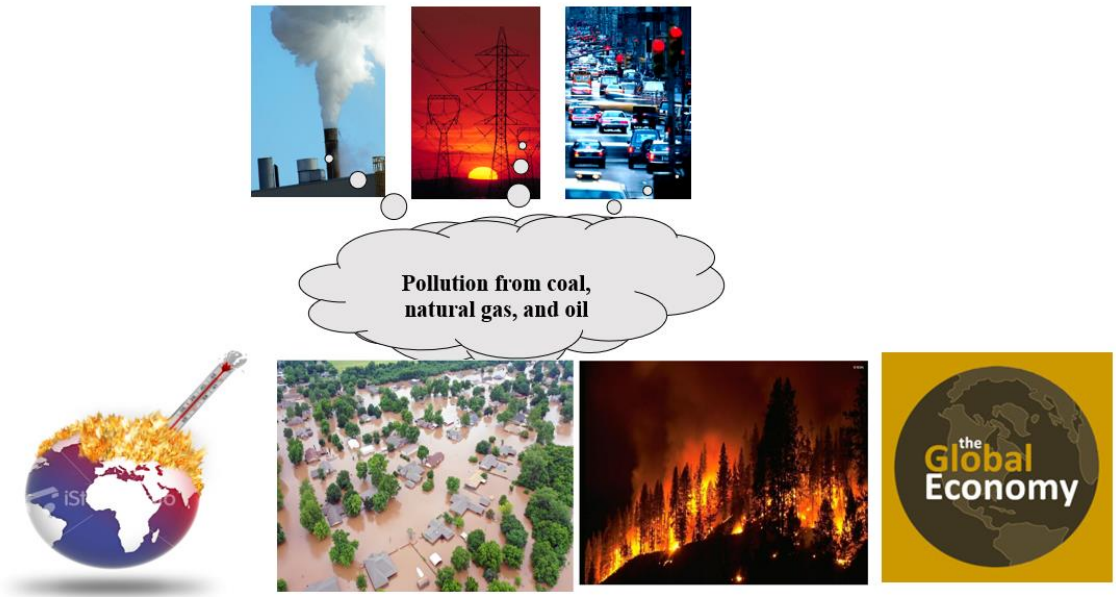

Figure 1. Global warming is due to carbon emissions and their effects on different aspects [5, 6].

1.2. Solar energy

The sun represents one of the major sources from which humans have attempted to produce energy over the centuries. While the sun is ~150 million kilometers away from earth, it constitutes a major source. In addition to the fact that it is inexhaustible, solar energy is easily accessible and clean. Only a small fraction of the sun's energy (1.2×10^{17} Js^{-1}) reaches the earth despite the enormous amount of energy it generates (8×10^{26} Js^{-1}) [8]. Surprisingly, this small fraction has great potential, as it would be greater than the total world's present electricity production capacity even if 0.1% of it could be transformed at 10% efficiency [9]. Figure 2 illustrates solar energy and its potential PV performance.

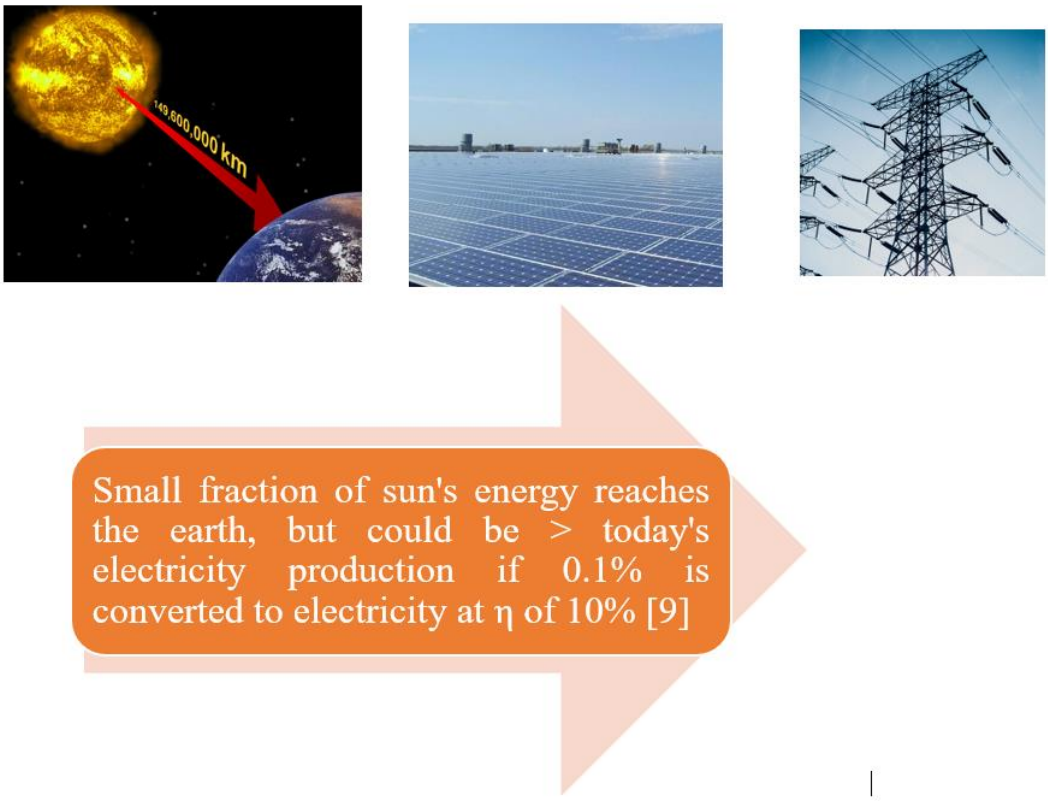

Figure 2. The potential of solar energy in energy conversion [8, 9].

As previously mentioned, the ever-increasing global energy demand has compelled researchers to continually develop and manufacture new generation and storage equipment. Photovoltaic (PV) devices represent an attractive technology capable of meeting some of the demands through the direct conversion of sunlight into electric power without emitting greenhouse gas (GHG). The PV effect was first observed in 1839 by Alexandre-Edmond Becquerel in an electrolyte solution, and in 1954 [10], Bell Labs revolutionized the industry by ushering in and developing the contemporary era of solid-state solar cells [10]. Since then, this technology has made profound efforts and inroads into becoming one of the most distinguished energy-harvesting techniques. Indeed, researchers have devoted themselves to its development. However, the technology's energy share has largely remained low. According to the International Energy Agency (IEA), PV share in global electricity

production currently accounts for only 3% [11]. In the short term, this limitation has been caused by the more costly nature of the common and commercially available silicon cells (Si-cells) than fossil fuels. Nonetheless, in the past few years, technological developments have dramatically reduced the cost of solar cell systems. Indeed, they have impressively grown and are expected to substantially exceed this limitation by 2040 to reach over 20% [12], as more efficient and less expensive PV technologies are aggressively being developed and improved. Although Si-cells is the most advanced, widely understood, dominant technology in the market (over 90%), and have reached a certified efficiency of over 25%, these devices have been associated with the high cost and this efficiency has been reported to be relatively low [12]. As such, to enhance competitiveness in this field, further research and development have been key. This research has led to the emergence and development of different PV technologies in recent decades. Our thesis pays attention to the understanding and development of two of these recent technologies, namely organic solar cells (OSCs) and perovskite solar cells (PSCs). Despite their potential to overcome the disadvantages and replace Si-cells highlighted above, they have been faced with stability problems. Accordingly, device encapsulation has been suggested as a technique to address this issue.

1.3. Purposes of this thesis

This work aims at improving the device stability and lifetime and understanding the impact that different encapsulation materials have on the aging rate of PSCs and OSCs. It extends the previous work by García-Encina in our Group of Optical Properties of Materials (GPOM) that focused only on OSCs and used Norland optical adhesives (NOAs) [13] by also investigating PSCs and incorporating an additional adhesive known as the Ossila encapsulation epoxy (OEE). Two NOA adhesives that provided the best encapsulation

performance in García-Encina's study, namely NOA 65 (a clear, colorless, liquid photopolymer) and NOA 71 (an optically clear, liquid adhesive).

The specific objectives in this thesis include:

- To fabricate inverted PSCs and standard BHJ OSCs.
- To characterize the prepared devices by *J-V* measurements and atomic force microscopy technique (AFM) for electrical and morphological characterization.
- To encapsulate PSCs and OSCs using three different adhesives, namely NOA 65, NOA 71, and OEE.
- To study the performance variation of different encapsulated cells with time.
- To identify the encapsulation material(s) that provides the best performance stability.
- To characterize the encapsulation materials using UV-Vis spectroscopy to evaluate their optical performance.

2. Theoretical background

This section introduces the current density-voltage characterization as well as the electronic and optical properties of organic and perovskite semiconductors. It reviews the devices' evolution, mechanism of operation, intrinsic properties, structures and architecture, and degradation mechanisms in turn. Finally, it discusses the state of the art of encapsulation in these solar cell technologies.

2.1. Current density-voltage (*J-V*) characterization

One of the vital characterization techniques used to describe device performance is that based on the *J-V* curves. The curves can be represented under either be illumination or not. When a solar cell photoactive layer absorbs photons under illumination, charge carriers are generated for extraction by corresponding electrodes due to the built-in electric field. This then creates a current in the external circuit. In the dark, both PSCs and OSCs display the behavior of a p-n junction diode, permitting the passage of electric current through the device upon application of some forward bias at the voltage for which the diode opens. The current passing through the device needs to be at its lowest when the applied forward or reverse bias is sufficiently close to the threshold voltage. Figure 3 shows the typical *J-V* characteristics of a solar cell with and/or without illumination. From this figure, a wide range of parameters detailing solar cell performance, including open-circuit voltage (V_{oc}), short-circuit current density (J_{sc}), maximal power point (MPP), fill factor (FF), and power conversion efficiency (PCE), can be extracted and are detailed in the paragraphs that follow.

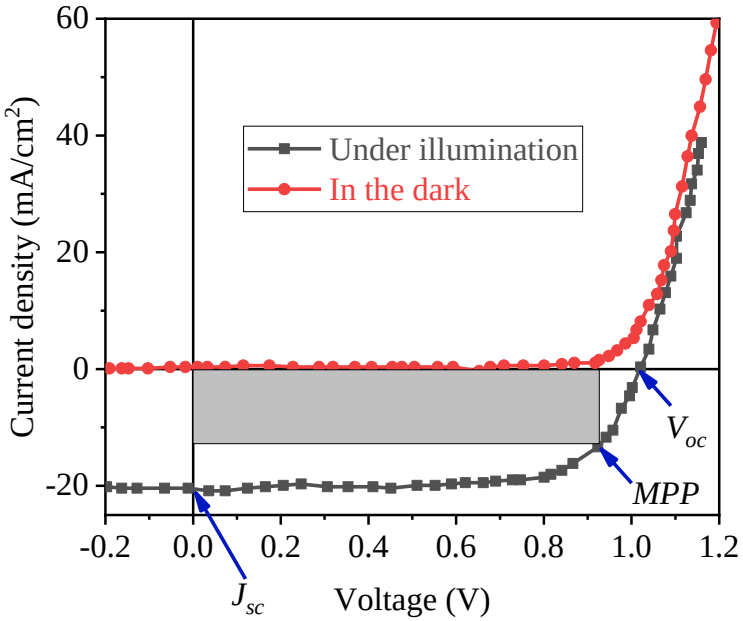

Figure 3. Typical J-V plots of solar cells under illumination (black) and in the dark (red). A solar simulator provided illumination. The key parameters are also shown in the curve [14].

Open circuit voltage (V_{oc}) refers to the voltage at which no current flows through the device under illumination. Differently from single junction inorganic cells where V_{oc} depends on the absorbing semiconductor bandgap, V_{oc} in bulk heterojunction (BHJ) OSCs is primarily determined by the energy difference between HUMO-LUMO offset at the device's donor-acceptor (D-A) interface [14]. Furthermore, the electrode nature and morphology and D-A blend morphology can cause slight variation between the experimental and theoretical values of this parameter [14]. Indeed, as effective charge separation processes lead to severe quenching of excited states at the interface of D-A, carrier losses result from non-radiative rather than radiative recombination pathways [14]. In PSCs, bandgap tuning and the ratio of charge carrier mobilities have a great impact on this parameter [14].

Short circuit current density (J_{sc}) can be defined as the current per unit area through the device under illumination when there is no external applied bias or when the voltage across it is zero ($V=0$). In OSCs and PSCs, this parameter essentially relies upon the donor material's light absorption, exciton/carrier generation, as well as exciton/carrier diffusion that depends on a particular material's diffusion length. It also depends on carrier mobility, which is determined by the active layer morphology and conductivity.

Maximal power point (*MPP*), as the name suggests, is the point at which the solar cell gives maximal power. **Fill factor (*FF*)** is the ratio of MPP and the ideal/theoretical maximum power obtainable (J_{sc}. V_{oc}) and is determined using Equation 1:

$$FF = \frac{J_{mpp.}\, V_{mpp}}{J_{sc}.V_{oc}} = \frac{MPP}{J_{sc}.V_{oc}.} \qquad 1$$

Where J_{mpp} and V_{mpp} are current density and voltage at MPP. Thus, FF indicates the PV cell quality and ranges from 0.75-0.80 [14]. It depicts the device *J-V* behavior deviation from ideality. Ideally, solar cells are modeled by a current source in parallel with a diode; however, no solar cells are practically ideal and components, including electrical resistances (shunt resistance (R_{sh}) and series resistance (R_s)) and ideality factor (n), are added to the model, remarkably affecting *J-V* behaviors deviations [14]. For example, lower R_{sh} and higher R_s reduce FF, thus lowering efficiencies. To improve efficiencies and thus lower R_s, it is important to accurately choose and process electrodes and buffer layers. Conversely, improving the active film morphology and controlling and tuning kinetics and energetics encompassing charge separation is crucial to minimizing shunt currents or increasing R_{sh}. Reinforcing these strategies can significantly optimize FF and efficiency in OSCs and PSCs.

Power conversion efficiency (PCE) is the ratio of the cell's electrical output power density at its maximum power point (P_m, in Wm^{-2}) to incident light irradiance (P_L, in Wm^{-2}), as Eq. 2 presents:

$$PCE = \frac{P_m}{P_L} = \frac{V_{oc} \cdot J_{sc} \cdot FF}{P_L} \qquad 2$$

For any particular PV cell, the conventional PCE is the efficiency measured under standard illumination conditions (incident radiation P_L = 100 $mWcm^{-2}$ and AM1.5 spectral shape) and temperature (25 °C) [14]. From the above equation, it is clear that efficiency is directly affected by factors, such as V_{oc}, J_{sc}, and FF. In addition, the area utilized for current density calculation can potentially influence PCE, and it ought to incorporate inactive areas that are fundamental to the device, including interconnects and grids, during efficiency calculation involving large areas. To contextualize the focus of this thesis, OSCs and PSCs are reviewed.

2.2. Organic solar cells (OSCs)

An OSC device is a type of next-generation or emerging solar cell in which an organic semiconductor – either small molecules or polymers – is the absorbing layer. The absorber layer is often sandwiched between the top low-work-function top electrode (cathode) and high-work-function anode. Normally, a hole transport layer (HTL) and an electron transport layer (ETL) are the interfacial layers and are placed between the anode and top electrode to enhance stability and performance. The detailed description of OSCs is described in the upcoming subsections.

2.2.1. Evolution of OSCs

OSCs trace their history back to 1906 when Pochettino observed photoconductivity in organic semiconductor materials, but numerous works were witnessed from 1970-1980

[15], where efficiency improvement from 10^{-5}-1% was reported. The achieved low efficiencies were due to low charge carrier mobility and concentration. However, two developments in the organic semiconductor field led to this efficiency improvement [15]. Firstly, the PV devices were applied with heterojunction, where high and fast quantum efficiency (QE) of electron transfer from excited polymers to acceptor C_{60} facilitated charge carrier separation. Secondly, the development of low-cost and efficient organic light-emitting diodes (OLEDs) enabled OSC testing and realization.

Fast-forward in 2001, an efficiency of up to 2.5% was reported [16], and seven years later, Kim, et al. reached an efficiency of 3.6% with CuPc/C_{60} bi-layer cell. Later, researchers used optimized structures and announced over 5% efficiency. In 2012, He, et al. found efficiencies as high as 9.2% with inverted structures for single-junction solar cells using PTB7/PC_{71}BM as the active layer material [17]. Tandem solar cells constituting multiple active layers with various bandgaps have been used as well to realize even higher OSCs efficiencies. Currently, certified efficiencies of 19% and 18.4% have been recorded for ternary and binary OSCs [18, 19], respectively.

High-performance small molecule donors/absorbers marked an outstanding OSC development. In the last decade, the field has been controlled by conjugated polymers. However, concerns linked to polymer synthesis, including batch-to-batch variation in performance, have compelled the need to look for small molecules to rival device polymers [15], as small molecules are unsuitably soluble for solution processing and vapor deposition are more costly hence less attractive. Despite the significant progress of vapor-deposited small molecules, many works have been excitedly attracted to solution-processable small molecule OSCs [20], which our thesis will specifically focus on for device processing.

2.2.2. Operation principles

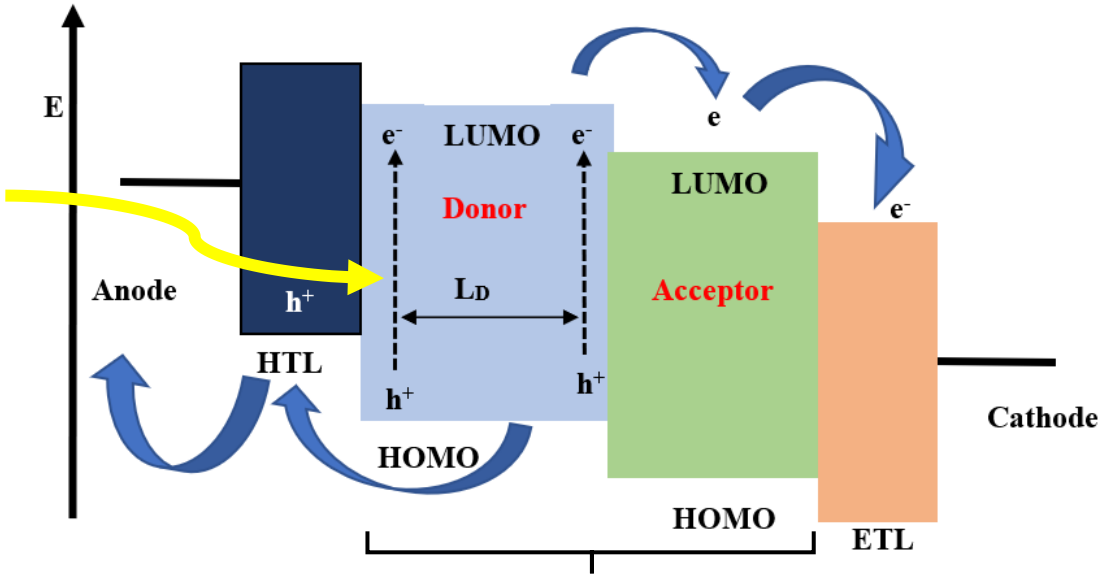

Active layer materials (D-A).

Figure 4. Mechanism of operation of OSC with standard (Anode/HTL/Active layer/ETL/Cathode or top electrode) structure. The yellow arrow indicates the incident beam, while the blue arrows show the movement/flow of holes and electrons [21].

The simplified operation principle of these types of solar cell technology can be described into four steps: photon absorption and exciton formation, exciton diffusion and charge dissociation, charge transportation, and charge collection [21, 22], as shown in Figure 4.

Photon absorption and exciton generation. The conjugated donor polymer of the BHJ absorbs the incoming incident photons from the anode side. The high absorption coefficient of these polymers (10^5 cm^{-1}) ensures that they absorb photons at the maximum of their absorption spectrum with a relatively thin photoactive layer thickness (100 nm) [22]. This thickness is also limited by the fact that the polymers have low charge-carrier mobilities ($10^{-4} cm^2 V^{-1} s^{-1}$ for holes and $2 \times 10^{-3} cm^2 V^{-1} s^{-1}$ for electrons) [18], resulting in absorption

of only a fraction of the incident light at absorption maximum and hence generation of low photocurrents because of the low conjugated polymer absorption [23]. However, the donor polymer bandgap can be lowered by using lower bandgap materials to improve absorption and optimize the number of harvested photons and improve efficiencies. Upon light illumination and photon absorption, the donor electrons are excited to their lower unoccupied molecular orbital (LUMO) from higher occupied molecular orbital (HOMO) and are likened to the promotion of electrons from the valence to conduction bands in inorganic semiconductors. Consequently, excitons, that is electron-hole pairs with relatively large binding energy (0.4–1.4 eV), are generated [24]. Afterward, the excitons migrate to the D-A interface.

Exciton diffusion and dissociation. In OSCs, excitons must overcome the relatively high exciton binding energy (0.3-0.5 eV) and dissociate into free charges to generate photocurrent. This dissociation occurs at the D-A interface [24]. As such, any formed excitons needfully move toward this interface through a diffusive process [21], in which they migrate from highly concentrated exciton regions to lowly concentrated ones. Two factors, namely film thickness and exciton diffusion length, L_D, influence the exciton diffusion efficiency [22]. Normally, the L_D is limited to a few nanometers and varies in the range of 5-20 nm, seriously limiting the absorber thickness. Excitons produced further away from the D-A interface > L_D, especially in thicker layers, will recombine, thereby reducing the conversion efficiency. After reaching the D-A interface, the excitons dissociate into free charges. This involves the initial transfer of excitons to the acceptor LUMO, leading to a charge transfer state (CT) or D^+-A^- or the polaron-pair state at the interface [25]. In the CT state, electrons and holes are situated at the D-A interface and are maintained in proximity by coulombic attraction [25]. Charges are completely separated in case the electron-hole-

pair-up size is larger than the Coulombic capture radius, the distance at which the two polarons are regarded to be freely generating electrons and holes.

Charge transportation. After dissociating into free charges, the independent electrons and holes occupy the acceptor and donor materials and move through the acceptor LUMO and donor HOMO, respectively, to establish a balance. The photoactive layer charge mobility, however, limits the charge carrier transport [21].

Charge collection. This is the final stage, and to circumvent recombination, buffer layers of HTL and ETL are used to discriminately ensure that holes and electrons reach the electrodes for collection by the bottom electrode anode and top electrode cathode, respectively. To ensure the electrodes efficiently perform their role of photocurrent collection, their work functions must be matched in the energetic level system [26].

2.2.3. Intrinsic properties

To become semiconducting or conducting, the organic light-absorbing materials need to have a high conjugation level or alternating single and double bonds [27]. Conjugation causes delocalization of the double bond electrons across the whole conjugation length, and compared to other molecule electrons, these electrons have higher energies and correspond to the inorganic semiconductor valence electrons. Nevertheless, the organic molecule electrons occupy HOMO rather than a valence band. At higher energies, organic semiconductors similarly have unoccupied energy levels as their inorganic counterparts, and the LUMO is the first one. An energy gap, also known as its bandgap, is situated between these two orbitals, and it reduces with increasing conjugation length [27].

Other than high conjugation, OSCs have also increasingly attracted attention because of other promising benefits, including low-temperature manufacture, tunable electronic properties, high absorption coefficient, solution processability, flexibility, as well as

lightweight, and semi-transparency [28]. They have continued to be superior despite having relatively lower efficiencies than other PV technologies due to low environmental impact, cost, and material toxicity [22]. To date, however, they have surpassed certified efficiencies of 18%, which is close to that attained by low-cost commercial devices based on silicon [22]. Besides, they have relatively poor stability, especially when under ambient conditions like illumination, high temperature, moisture, oxygen, etc. [22]. This thesis seeks to address the lifetime challenge through encapsulation as barriers, as discussed more extensively in the subsequent subsections.

2.2.4. Structure and architecture

These PV technologies can be fabricated in either standard (direct) or inverted (inverse) configurations [28]. In the standard configuration (Figure 5a), the anode is made of transparent conductive oxide (TCO) which serves as the positive electrode permitting light passage and hole collection. An HTL, which discriminately blocks electrons from reaching the anode and reduces the direct diffusion of degrading anode material to the photoactive layer, is deposited on top of the TCO-coated glass substrate. The photoactive layer is deposited on the HTL, and then, the ETL is deposited on the photoactive layer. Different materials, including poly[(9,9-bis(3′-(N,N-dimethylamino)propyl)-2,7-fluorene)-alt-2,7-(9,9-dioctylfluorene)] (PFN) or calcium, may be used for this layer. Finally, aluminum or silver can be used as top electrodes. By contrast, in the inverted configuration architecture (Figure 5b), the negative back electrode is made of the TCO and the positive anode is at the top electrode [29]. Notably, TCO now becomes the cathode, and light enters into the device from the bottom electrode side. Therefore, for photogeneration to occur in the inverse configuration, the cathode and ETL must be semitransparent. In this structure, the fullerene layer is covered by several layers that minimize its exposure to ambient factors [28]. In

addition, it makes it possible to use different air-stable materials as top electrodes [30]. Thus, it considerably improves the OCS durability.

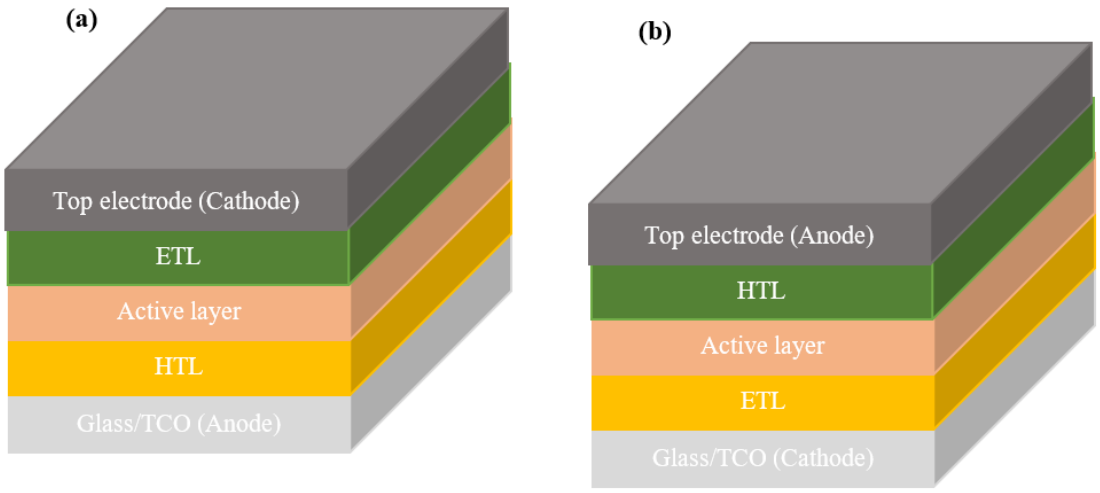

Figure 5. OSC structures (a) standard (direct) and (b) inverse configuration [28].

The active layer, regardless of the configuration under scrutiny, can be fabricated using bi-layer [31], BHJ [32], or tandem [33] structures as shown in Figure 6. In a bi-layer structure, the electron donor and acceptor layers are placed side by side as independent layers (Figure 6a). Just like a p-n junction Si cells have, the bi-layer structure has a low exciton diffusion length (~5-20 nm), whilst the polymer donor layer thickness required for efficiently adequate light absorption is 100 nm. As such, a better and more efficient structure to intimately disperse the donor and acceptor materials throughout the photoactive area that greatly enhances the interfacial area is necessary and is called BHJ structure (Figure 6b). This structure is advantageous in that it needs a smaller exciton diffusion distance, efficiently dissociating excitons in OSCs [32]. Accordingly, the photoactive layer donor and acceptor phase arrangement, called the morphology, is innate for an OSC electronic performance.

Although less common, the tandem structure (Figure 6c) includes a sandwich of stacked OSCs in parallel or series and improves the absorption range of the photoactive layer, and produces larger V_{oc} values. However, joining the devices and selecting effective and well-performing materials is usually a challenge [33]. In this thesis, the most commonly used configuration for research, binary active BHJ layer, was considered.

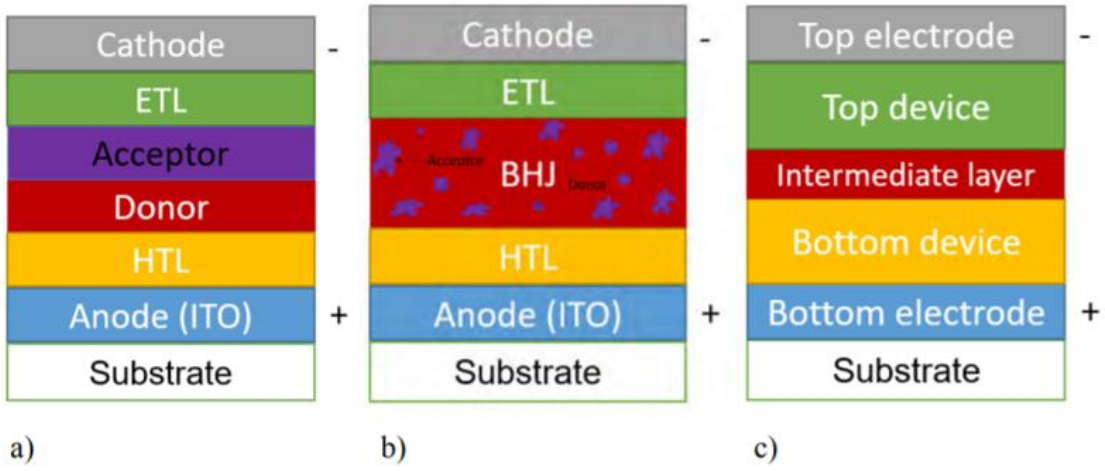

Figure 6. OSC active layer structures (a) bi-layer, (b) bulk-heterojunction (BHJ), and (c) tandem structure in direct configuration [31-33].

2.2.5. Stability and degradation processes

In OSCs, degradations can be either chemically or physically induced. In chemical degradation, extrinsic degradation involving molecular moisture and oxygen diffusion into the cells is the most critical degradation factor. Due to the sensitivity of organic materials to these components, the organic layers and interfaces undergo photooxidation, affecting their optical and electrical properties [34, 35]. Metal electrodes are similarly photo-oxidized to form metal oxides that act as carrier transport barriers at the interface between the metal and other device layers. As will be described in subsection 2.4.1, encapsulation barriers can be instrumental in reducing extrinsic moisture- and oxygen-induced degradation but not the dangerous intrinsic degradation sources such as ultraviolet (UV) light. The UV light causes

photochemical reactions, as its energy is adequate to break up the organic materials' carbon bonds, with dissociation energy of ~3.5 eV. Since they can filter the UV, encapsulation materials can mitigate this harmful solar spectrum range [34]. Fullerene photo-oligomerization, particularly $PC_{61}BM$ and C_{60}, is the other source of intrinsic chemical degradation that causes burn-in losses in these types of devices [35-37].

HTL, especially PEDOT:PSS used in this thesis, also contributes to OSC degradation. Owing to its hygroscopicity nature, PEDOT:PSS may speed moisture permeation throughout the device, thereby serving as a water source for other degradation processes in adjacent layers [36]. In addition, the material is acidic and can cause ITO etching using the classical structure where there is contact between the two materials, particularly in the presence of water [34]. Surfactant additives in PEDOT:PSS commercial formulations may diffuse to the layer surfaces, thus impacting the adjacent layer interfaces [34].

In addition to extrinsic and intrinsic chemical degradation, physical degradation encompassing mechanical failures may occur in the device stack. Under thermal stress, encapsulation failure by delamination of flexible OSC multiple thin-film layers might happen [34]. Extrinsic and intrinsic physical degradations are delamination and morphological stability. Upon illumination, OSC heats up and causes the device nanostructure rearrangement in the buffer or active layers. This modification can potentially segregate interfaces, impeding charge extraction. Ultimately, the donor and active materials can undergo phase separation so that the distance between them becomes larger than the exciton diffusion length, hampering free carrier generation [38]. For small molecular acceptors in the blend, heating temperatures higher than the glass transition temperature, T_g, can cause degradation through morphological changes (aggregation surrounded by depletion zone)

with the potential to decrease the D-A interface areas [38], thus hindering the exciton separation and charge transport in the photoactive layer.

2.3. Perovskite solar cells (PSCs)

2.3.1. Evolution of PSCs

Perovskite materials have been widely investigated since 1839 when Gustav Rose, the Russian mineralogist, discovered the first perovskite material known as calcium titanate ($CaTiO_3$) [39]. It was until recently, however, that researchers actively commenced the material's semiconductor applications. In PV, researchers initially began using perovskites in the form of dye-sensitized solar cells (DSSCs). In 2009, Kojima et. al. initially employed a perovskite material, methylammonium lead tri-iodide ($MAPbI_3$), as a light harvester and achieved an efficiency of 3.8% [39]. Although this efficiency later increased to 6.5% through the liquid electrolyte $MAPbI_3$ quantum dots processing [40], it was faced with poor stability, and with the inclusion of a solid-state hole-transporting material, Spiro-OMeTAD, the efficiency improved to about 10% in 2012 [41]. With devoted efforts that involved a planar configured solar cell with compositional engineering of the active layer, the device efficiency was increased to ~15% [42]. The better efficiency was a result of enhanced homogeneity of the perovskite film and increased carrier diffusion length. Recent advancements by various research groups have led to great progress and have attained a considerable efficiency improvement. For instance, Ulsan National Institute of Science and Technology (UNIST) has recently reported efficiency of more than 25% [43]. However, lower PCEs varying between 10% and 15% have continuously been presented. Figure 7 shows the NREL chart efficiency history for the different kinds of solar cells, where it is evident that PSC efficiency has risen more dramatically within just a decade since it was first used in solar cells.

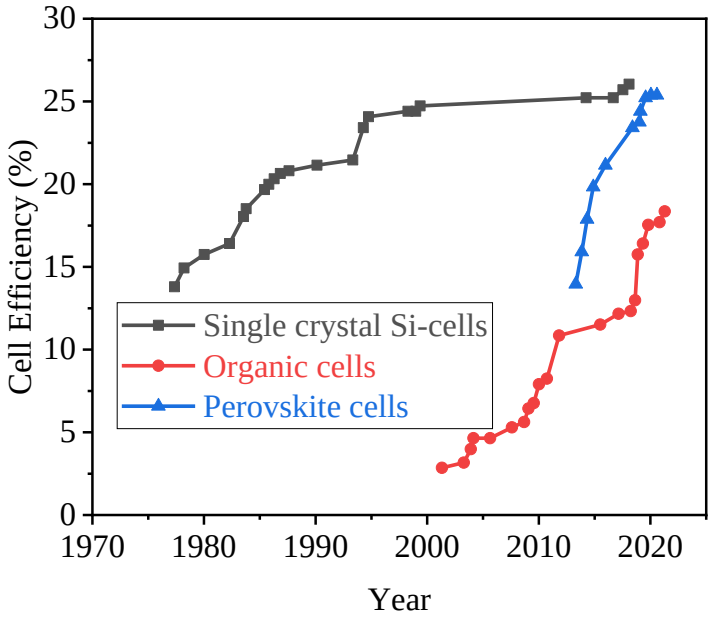

Figure 7. Best research-cell PCE history chart [43].

2.3.2. Operation principles

The working principle of PSC similarly involves four steps just as is the case with OSCs, but they differ in charge generation. Here, the active layer (perovskite material) is in a crystalline phase contrary to the OSC active layer, which is amorphous. This brings some specific characteristics for charge generation and transport. The other steps include photon absorption and charge generation, charge separation, charge transportation, and charge collection. Figure 8 indicates the steps involved in inverted PSC operation.

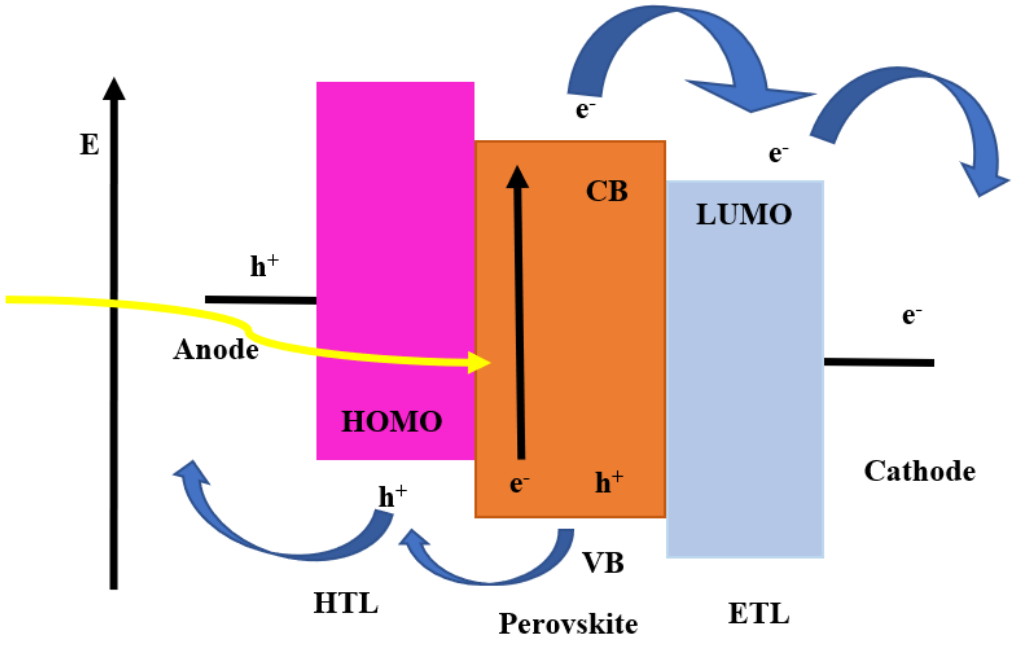

Figure 8. Mechanism of operation of PSCs with inverted p-i-n (Anode/HTL/perovskite/ETL/cathode) structure. The LUMO, HOMO, conduction band (CB), and valence band (VB) are aligned to the vacuum, the electron and free space property employed in alignment level for two different materials energy levels. The yellow arrow indicates the incident beam, while the blue arrows show the flow of holes and electrons [44].

Photon absorption and charge generation. Like OSCs, perovskite materials, for instance, $MAPbI_3$, have high absorption coefficients (10^5 cm^{-1}) in the Vis region, direct bandgap (~1.55 eV), and absorption onset of approximately 800 nm [21]. Relatively thicker active layer films (~300-500 nm) than OSCs (100 nm) [21], respectively) can efficiently harvest the incident light and transform it into electric energy because of lower binding energy than OSCs (<0.05 eV), greater carrier mobilities (2-10 $cm^2/(V{\cdot}s)$ for electrons and 5-12 $cm^2/(V{\cdot}s)$ for holes), and larger L_D than OSCs [44]. In contrast to OSCs, photon absorption in perovskites does not result in large lifetime exciton creation. Instead, it advantageously leads to direct and efficient generation of free charges in a single step, as excitons cause considerable energy losses through their migration and dissociation [44, 45].

Charge separation. After light absorption and charge generation, the charges are separated either through the injection of photo-generated electrons into the ETL or injection of photo-generated holes into the HTL. These injections have been found to happen in similar timescales of sub-10-ns timescales [46]. Additionally, free electrons formed closer to the perovskite/HTL interface must move diffusively across the absorber width for extraction at the ETL/perovskite interface. This event is associated with increased recombination probability. Similar considerations apply to holes closer to the ETL/perovskite interface.

Charge transportation. After charge separation, the carrier transport occurs, in which free holes next to the ETL/active layer interface are extracted at the HTL/active layer interface after diffusing through the active layer. This process may potentially cause recombination. Next, these holes pass through the HTL and are transported to the HTL/electrode interface. In the same manner, a similar process takes place for electrons situated next to the ETL/active layer interface. To promote the charge transfer, it is important to use charge transporting materials (CTMs) with a good match of HOMO and LUMO levels, which means corresponding well with high-work-function (e.g., Au) and low-work-function metals (e.g., Al), respectively, with similar energy levels.

Charge collection. This is the final stage involving the extraction of free holes and electrons at the HTL/electrodes and ETL/electrodes interfaces, respectively. For efficient transfer of holes or electrons, the drop-casted, printed, or evaporated electrodes must necessarily possess ideal work functions. They also need to show intrinsic stability towards ambient components such as moisture and sunlight to enhance the device lifetime.

2.3.3. Intrinsic properties

Figure 9 shows the crystalline structure of hybrid organic-inorganic perovskite semiconductor materials. These materials have many exciting physical properties, namely

high absorption co-efficient, long carrier diffusion length, low exciton binding energy, tunable bandgap, as well as flexible and facile processing [47-49], which make them suitable for PV applications. As shown in Figure 6, perovskites take the structure ABX_3, constituting an organic or inorganic monovalent cation, A = formamidinium (FA) $CH_3(NH_2)_2^+$), methyl-ammonium (MA) CH_3NH^{3+}, n-butylammonium (BA) $CH_3(CH_2)_3NH_3^+$, ethyl ammonium (EA) $CH_3CH_2NH_3^+$, and Cs^+, ethylammonium; a divalent cation, B = (Pb^{2+}; Ge^{2+} and Sn^{2+}), and an anion X = (Cl^-; Br^-; I-; SCN^-; BF_4^- and PF_6^-) [50-51].

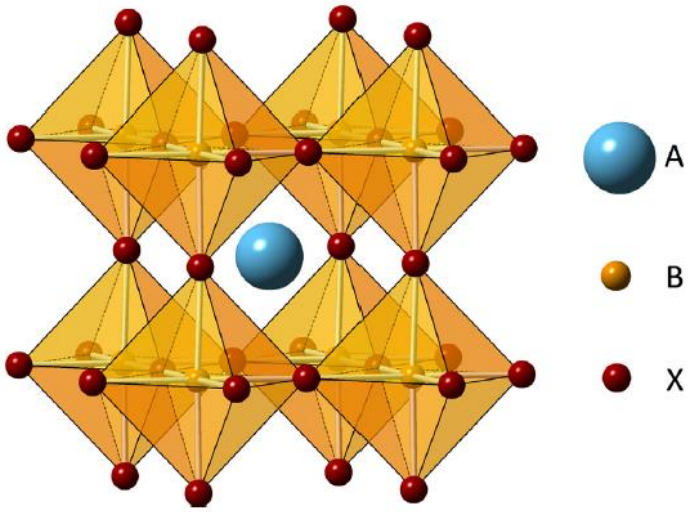

Figure 9. Crystalline structure of the hybrid organic-inorganic perovskite, in which A is a monovalent cation, B is a divalent cation, and X is a monovalent anion [49].

PSCs can have different crystal structures, including 0-D (all dimensions are measured within the nanoscale and none is larger than 100 nm), 1-D (one dimension is outside the nanoscale), 2-D (two dimensions are outside the nanoscale), and 3-D (no dimension is confined to the nanoscale) [49-50]. Regarding perovskites, examples of these crystal structures, respectively, are $CH_3NH_3PbI_3$, $(CH_3NH_3)2PbI_4$, $(C_{10}H_{21}NH_3)_2PbI_4$, and $(CH_3NH_3)_4PbI_6{\bullet}2H_2O$ [21]. Currently, 0-D perovskites are the most commonly utilized, and their bandgaps can be tuned through cation or anion substitution. Markedly, compared to

other structures, 2-D PSCs show greater chemical stability and photo-stability during operation. However, its PCE is significantly lower than its counterparts. Tremendous efforts have been made to improve perovskite performance [21]. For instance, to attain the PCE-lifetime trade-off, researchers have recently integrated different structures.

2.3.4. Structure and architecture

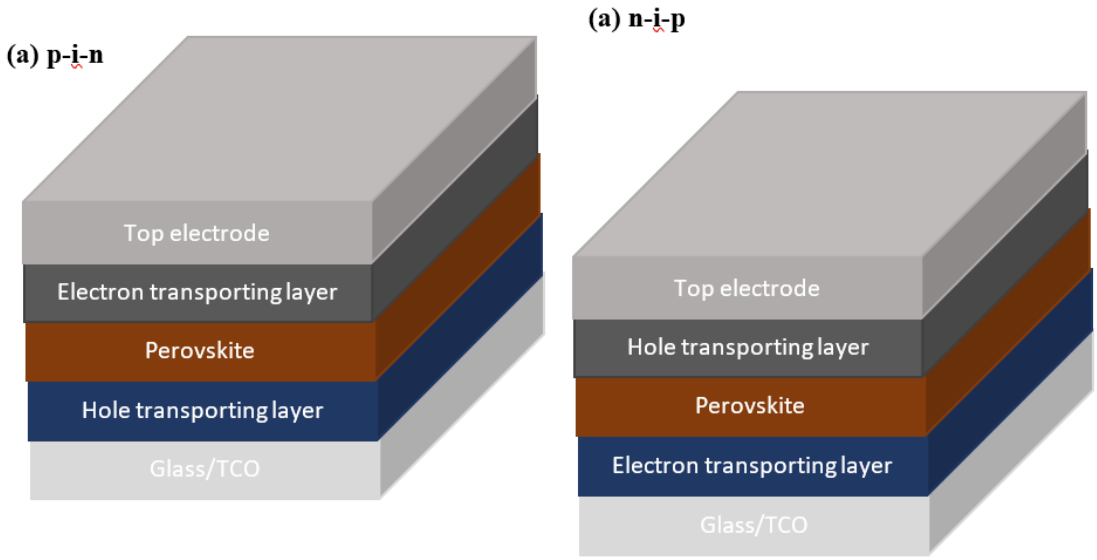

Figure 10. Different types of PSC architectures: (a) inverted p-i-n architecture; and (b) direct n-i-p architecture [51].

As shown in Figure 10, PSCs can fall into two types of architectures, the p-i-n and n-i-p architectures. In the p-i-n or inverted architecture, HTLs such as PEDOT:PSS or NiO are first deposited on the TCO-coated glass substrates, such as FTO or indium-tin-oxide (ITO), and annealed to obtain mesoporous or planar films [51, 52]. The perovskite film is then processed on the HTL and annealed. Afterward, the ETL such as ZnO, [6,6]-phenyl-C61-butyric acid methyl ester (PCBM), SnO_2, or TiO_2, is deposited on the perovskite before drop-casting or evaporating low work-function metals like silver or field's metal (FM). In contrast to the p-i-n, the n-i-p architecture involves depositing ETL on the TCO-coated glass substrate

before fabricating and annealing the perovskite layer on it. Then, a HTL such as spiro-MeOTAD is deposited on the perovskite layer. To complete the PV fabrication, a high work-function metal such as Au or printing carbon electrodes are evaporated on top [51]. For our thesis, the inverted PSC architecture was fabricated.

2.3.5. Stability and degradation processes

Device degradation remains one of the concerns that PSCs have continued to experience, thus adversely impacting their stability and commercialization. These processes have been reported to be induced through three main methods, including moisture, oxygen, thermal, and light [52, 53]. Concerning moisture-induced degradation, studies are still investigating to precisely establish how moisture causes degradation of this novel PV technology. When exposed to ambient atmosphere, water, as a Lewis base, and perovskite material can irreversibly react and degrade via coordination between the proton of ammonium in $CH_3NH_3PbI_3$ and the H_2O [54]. Whereas earlier studies have reported the PbI_2 formation and methyl-amine loss, the latest reports have recently implied an intermediate step involving the partial and reversible formation of $(CH_3NH_3)_4PbI_6{:}H_2O$ hydrate complexes that then disintegrate further into PbI_2, HI, and CH_3NH_2 [54, 55], as shown in Figure 1. Equations below provide the process of decomposition when moisture and oxygen are involved in PSC degradation.

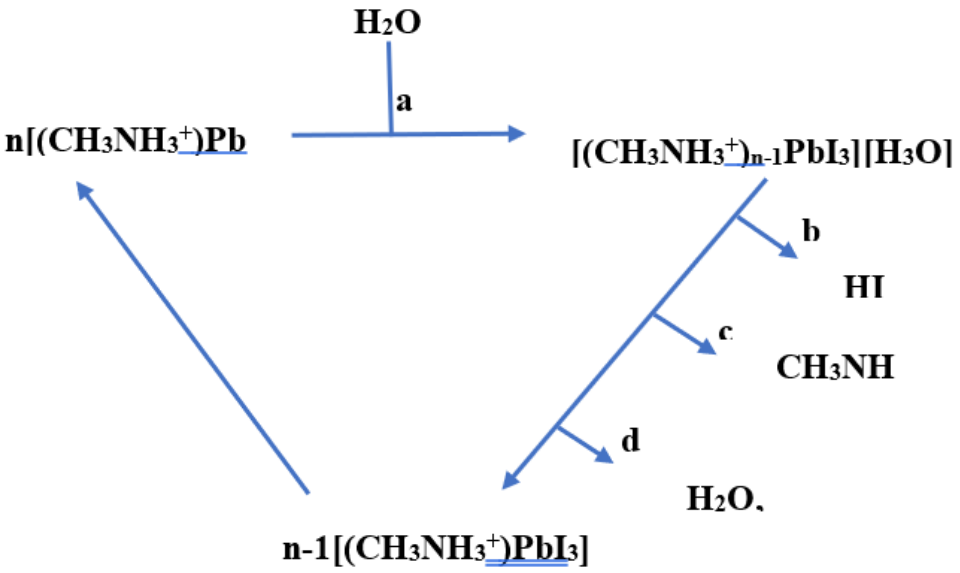

Figure 11. Schematic illustration of degradation process between hybrid perovskite and moisture. The reaction and the resulting products, including hydrate complexes, CH_3NH_2, and HI [54, 55].

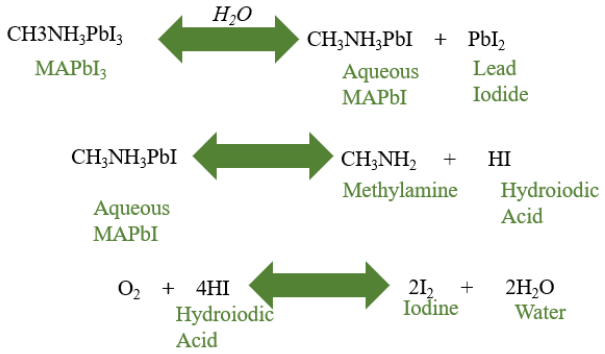

Thermally-induced degradation resulting from high temperatures is another source of device instability. Studies have shown that heating perovskite materials such as $CH_3NH_3PbI_3$ to higher temperatures, > 150 °C, can lead to a reversible degradation process [51, 56]. Under such thermal stress, $CH_3NH_3PbI_3$ undergoes endothermic reaction, decomposing into PbI_2, HI, and CH_3NH_2. By contrast, the reaction between PbI_2 and CH_3NH_3I may occur, thus forming new perovskite compounds, $CH_3NH_3PbI_3$. Finally, photo-induced degradation during exposure to the environmental atmosphere has been cited as among the key reasons for short methyl ammonium (MAI or $CH_3NH_3PbI_3$) perovskite lifetimes. Indeed, Ouyang, et

al. and Wang, et al. observed that PSCs quickly degraded within several minutes to hours when they exposed the devices to light and dry air [57, 58]. Chen speculated this fast degradation to the reaction between photo-generated electrons and oxygen, forming superoxide to deprotonate the $CH_3NH_4^+$ degrading the perovskites [59]. To suppress light-induced degradation, therefore, encapsulating devices in the glove box with an inert atmosphere is recommended.

Light irradiation is the other concerning factor causing degradation and instability since device electricity generation requires that they must encounter illumination and electrical bias. In PSCs, some materials used as ETLs act as photocatalysts. For instance, TiO_2, with a redox property and bandgap of 3.2 eV, has been reported to act this way. In addition to oxidizing water to yield OH radical, TiO_2 oxidizes some organic materials [58]. Wang, et al. pointed out that under UV illumination, Titania photoanode displays quick PCE decay even when encapsulated in an inert atmosphere; by contrast, in open-air conditions, unencapsulated PSCs exhibit better stability since atmospheric factors eliminate surface state from titania [58]. This explains that PSC degradation arises because of UV irradiation, thereby affecting the titania layer, and is attributed to light persuaded desorption of the surface-induced oxygen. Recent reports have explained that fabricating devices expose them to open air, and the deep traps are passivated due to the oxygen adsorption [59].

In summary, both PSCs and OSCs have instability concerns resulting in degradation. Factors, such as moisture, oxygen, light, UV light, and high temperatures, are the major contributing components, resulting in absorption losses and forming shallow or deep trap states leading to recombination and causing performance loss by reducing the operating performance parameters and increasing the system energetic disorder. Research has extensively been conducted to minimize photochemical reactions, with most efforts being

directed to addressing intrinsic degradation within the device layers, including interface engineering, electrode engineering, and compositional engineering [60]. This thesis, however, pays attention to extrinsic degradation prevention majorly due to water and oxygen, and encapsulation has been suggested as a good strategy to reduce this type of degradation by preventing the entry of moisture and oxygen into the device. The next subsection turns its focus on discussing the concept of encapsulation and how it can affect device stability and lifetime.

2.4. State of the art device encapsulation

2.4.1. Role of device encapsulation

Device encapsulation is a technique used to protect solar cells against external stressors and ascertain that they perform reliably and durably [60]. Typically, extrinsic instability encompassing external environmental factors namely oxygen, water, incident light particularly UV light, scratches, and combinations thereof, have the potential to damage both PSCs and OSCs when present in certain amounts and cause performance attenuation. This is exacerbated by the fact that these solar cells are sensitive to these factors. While interface, compositional, and electrode engineering methods are pivotal in improving internal or intrinsic stability and performance, encapsulation is an effective way to significantly reduce extrinsic or external instability to attain economically feasible and practicable cells [60]. To improve lifetimes, encapsulation materials enhance scratch resistance and mechanical stability [60]. Device encapsulation also serves to safeguard against aging factors like moisture and oxygen, which are the two main sources of degradation, as well as protect them from UV radiation as the materials also act as UV filters [61]. While the protective barrier would ideally function to seal these cells in a glass container with an inert atmosphere aimed

at complete exclusion of the ambient elements responsible for degradation, this is impractical in many circumstances.

Irrespective of the encapsulation technique used, the main ambient degradation components, oxygen and moisture, can permeate into the device through two pathways, which multiple reports have referred to as lateral and orthogonal permeation [62]. On the one hand, lateral permeation, commonly known as side ingress, is a permeation that occurs in the device plane. On the other hand, orthogonal permeation is that which takes place orthogonally to the device plane. Figure 12 illustrates these two major types of permeation pathways. Numerous encapsulation schemes, owing to the inherent OSC devices' aspect ratio (evidenced in their large area and small thickness), make use of some form of a stack with the cell at the center [62], creating interfaces that offer lateral permeation. Resultantly, this permeation can be further classified into interface permeation and bulk permeation via a material [62].

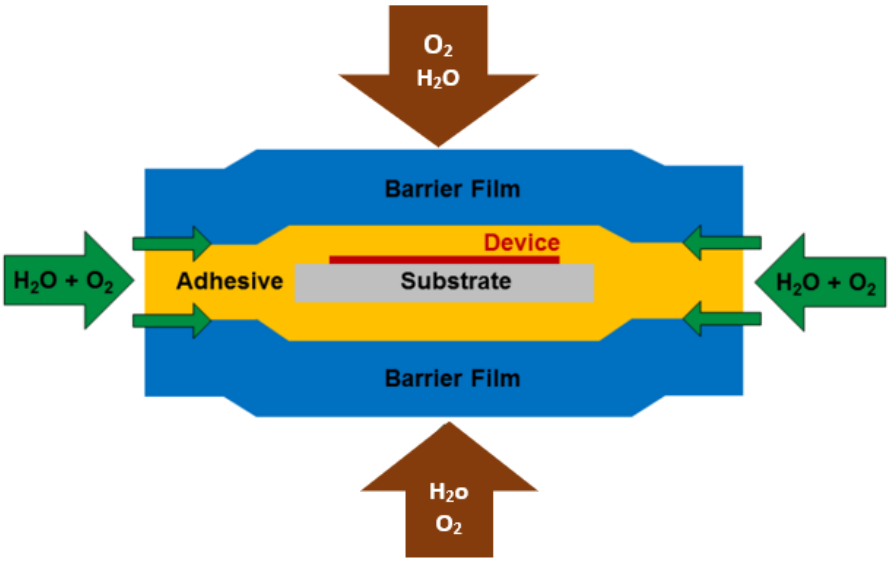

Figure 12. Permeation pathways for oxygen and moisture for a typical device encapsulation scheme. The green arrows show lateral permeation that might take place either through the interfaces or the bulk adhesive, and the brown arrows indicate orthogonal permeation [62].

2.4.2. Properties of encapsulation materials

Different encapsulation materials have been suggested for use in the PV module. However, these materials should meet certain requirements to efficiently carry out their functions and attain commercialization. The requirements in terms of module efficiency optimization can be categorized into various divisions, including reliability, electrical safety, electric yield, module processing, and cost [51, 60, 63]. First, the encapsulation materials have to offer high transmittance/low absorption as well as an adapted refractive index to reduce interface reflectance. Second, the materials should have high thermal conductivity to minimize operating temperatures and improve electric yield thus circumventing the deterioration of cell performance. Third, they should only allow very low leakage currents to ensure electrical safety. Fourth, they should mitigate external stresses such as moisture, oxygen, heat, mechanical loads, UV irradiation, electric potential relative to the ground,

among other factors to ascertain PV module reliability. The materials ought to maintain strong adhesion to other device elements as well as safeguard them from external impacts. They should have high barrier performance to oxygen and water. To warrant optimal encapsulation performance, the water vapor transmission rate (WVTR) and oxygen transmission rate (OTR) have to be in the order of 10^{-3}–10^{-6} $gm^{-2}d^{-1}$ and 10^{-4}–10^{-6} $cm^3m^{-2}d^{-1}atm^{-1}$, respectively [60]. An encapsulation material's barrier performance levels have a strong influence on the device's lifetime, as the rate at which efficiency declines depends upon the barrier-sealant OTR and WVTR [60]. Finally, they need to have low processing time, processing cost, and material cost for mass production.

Based on the requirements highlighted above, Table 1 shows certain crucial aspects that must be considered when selecting suitable PV encapsulants. In addition to the basic material properties, including melting temperature T_m and glass transition temperature T_g, the mechanical properties are also vital to attain buffering properties of withstanding mechanical impacts as well as thermomechanical and mechanical loads [63].

Table 1. Overview of the crucial parameters of encapsulation evaluation [63].

Parameter	Relevance
Young's modulus *E*	Mechanical stress on the module
Melting temperature T_M	Processability
Glass transition temperature T_g	Limited material property variation within the exposure temperature range
Refractive index *n*	Minimizing optical losses
Volume resistivity	Electrical insulation
Absorption	Minimizing optical losses
WVTR **OTR**	Knowledge concerning mass transport processes within the cell

2.4.3. Encapsulation strategies and packaging systems

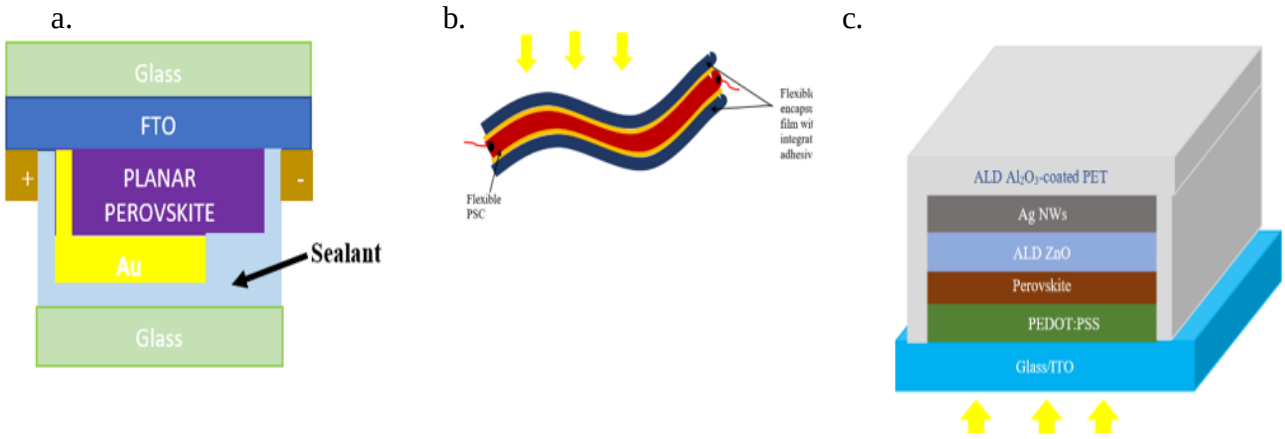

Figure 13. Different encapsulation methods. ***(a)*** *Glass-to-glass encapsulation.* ***(b)*** *Polymer encapsulation.* ***(c)*** *Thin film encapsulation [51, 63].*

Figure 13 shows the different and suitable and efficient encapsulation schemes that have been implemented with different levels of success. They include polymer

encapsulation/flexible encapsulation, thin-film encapsulation, and glass-to-glass encapsulation [51, 63]. Glass-to-glass encapsulation (Figure 13a), which was adopted for use in this thesis project, is the most common method, and it entails encasing the device between two glass sheets, in which one of the glasses is the device substrate, using glue for edge sealing [64]. Employing this encapsulation technique, studies have reported considerable lifetimes of up to 5600 h for organic light-emitting diodes (OLEDs), even though OLEDs require more stringent penetration rates for water and oxygen penetration rates compared to OSCs and PSCs [65]. While device flexibility is compromised when utilizing rigid glass-glass encapsulation, this technique also offers other benefits, such as extremely low WVTR and OTR, which flexible alternatives have not been able to match.

Other than rigid glass-to-glass encapsulation, flexible encapsulation (Figure 13b) involves polymer encapsulation approaches using R2R processing. One of the materials that were initially examined for this scheme of device protection was polyethylene terephthalate (PET), a common thermoplastic polymer resin. However, the findings were unpromising as the researchers found that rather than improving the device lifetime, PET notably reduced it instead [66]. Later research utilizing R2R processing similarly employed PET substrates but found that encapsulated films had successfully reduced degradation [67], as lifetimes in hundreds of hours and tens of hours in a dry nitrogen atmosphere and air, respectively, were established.

More recently, thin-film/direct encapsulation methods (Figure 13c), such as Atomic Layer Deposition (ALD) and multilayer dyad structures, have been developed and implemented [60]. Instead of depending on lamination, this scheme allows for the direct building of barriers on top of cells. Similar to the flexible film technique, it not only provides

orthogonal protection but also extends to limit lateral permeation based upon the scheme that has been used.

To reliably and effectively encapsulate PV modules, the selection of an appropriate patterning strategy is a critical aspect. It is important to design the encapsulation pattern in such a manner as to avoid any photochemical and/or thermal damage to the solar cells, suppress oxygen/moisture penetration, and guarantee long-term stable adhesion to the PV module in harsh weather conditions. Based on this context, Aranda, et al. and Matteocci, et al. have classified device packaging systems into top encapsulant barriers and edge sealing [68, 69]. While the former involves the deposition of a thin protective layer on top of the device, the latter entails the placement of the sealant around the module bonded to a cover substrate. Compared to cover barrier or top encapsulation, stability tests have established that edge sealing has greater reliability because it suppresses and prevents the effects of side penetration [60]. Our thesis, however, considered implementing blanket encapsulation patterns, which have been shown to offer better barrier performance than the other two, as it integrates both edge sealing and cover barriers and exploits their advantages. It creates a pressure-tight environment that serves to not only blocks the ingress of environmental moisture but also prevents any volatile materials from escaping the module. As such, the blanket strategy is the most reliable and effective encapsulation packaging for the long-term, stable of PSCs and OSCs [61, 70, 71]. Figure 14 shows the different packaging systems of PV devices.

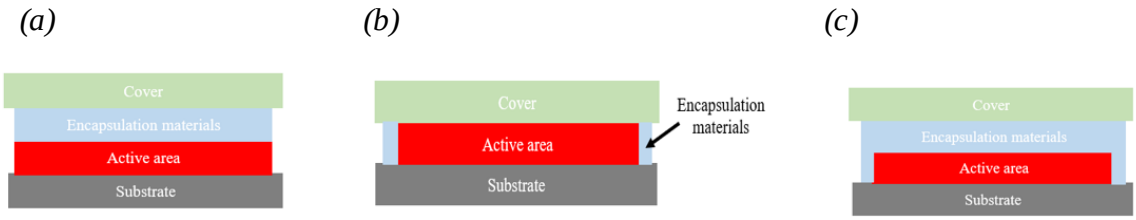

Figure 14. ***(a)*** *Protective layer as encapsulation materials covers the active area.* ***(b)*** *The sealant is placed on the edge of the active area. (c) Blanket encapsulation integrates barrier and edge seals [68, 69, 71].*

2.4.4. Device stability and lifetime

Despite the innumerable advantages these devices offer over the current commercial solar cells, extrinsic stability has been unsatisfying. Although researchers have made tremendous efforts in recent years to improve intrinsic instability through compositional engineering, interface engineering, electrode engineering [58]. The establishment of the most effective encapsulation material to minimize external device stability remains insufficiently investigated [63, 64]. Against this backdrop, this work designed OSCs and PSCs, encapsulated them with different encapsulants, and compared the materials' performance to identify the best among them. Few researchers have attempted to address this comparison problem using other adhesives. For instance, Cheacharoen et al. compared ethyl vinyl acetate (EVA) and Surlyn to assess their barrier performance on PSCs and found that EVA outperformed Surlyn [72]. The authors attributed EVA's performance to its low Young's modulus that dispersed the strain. EVA and Surlyn are, however, unsuitable to OSCs and PSCs, as they produce harmful byproducts to the devices when used. Others have compared epoxy and other UV-curable adhesives and have revealed the former to offer better barrier protection than the latter [71].

Many new encapsulation materials have recently been suggested for use in these devices but are yet to be compared. Indeed, Li, et al. emphasize the urgent need to compare stability findings from various labs across the globe, as the present stability tests, especially of PSCs, are chaotic and adapted from silicon modules, which, nevertheless, are ostensibly much different from the perovskites and to some extent OSCs [71]. García-Encina's thesis in GPOM Group recently focused on encapsulation of OSCs using NOAs only [13] and found that devices with NOA 65 and NOA 71 achieved the best stability. Thus, it is imperative to extend this study to not only include other device types (PSCs) but also utilize different encapsulation materials.

3. Experimental methods

This chapter introduces the materials, fabrication processes, and characterization methods for OSCs and PSCs used in this thesis project. It also discusses the UV-Vis spectroscopy technique as a method to assess the optical performance of the utilized encapsulants in the device encapsulation.

3.1. Organic solar cells (OSCs)

3.1.1. Materials

PEDOT:PSS (Clevios PVP AI4083) was obtained from Heraeus-Clevios and was used as received. Phenyl-C70-butyric acid methyl ester (PC70BM) was received from American Dye Source. Solvents used for this work included methanol and acetic acid, and chlorobenzene (CB), which was acquired from Sigma Aldrich. A substrate-device glass/ITO with 10-15 Ω/square was purchased from Delta Technologies. On the other hand, new materials that were used specifically in OSC fabrication were poly(3- hexylthiophene) (P3HT) from one of my thesis advisor's co-workers and PFN from Sigma-Aldrich. The eutectic alloy Field's metal (FM), used as the back electrode, was acquired from Rotometals. The FM has been utilized as an alternative top electrode by previous GPOM researchers in their works [73-75]. It constitutes bismuth (Bi), indium (In), and tin (Sn) with the following weight fractions: 32.5, 51%, and 16.5%, respectively, and has a low melting point (62 °C). Unlike other standard top electrodes which are more costly due to high-vacuum evaporation, FM can be drop-casted at low temperatures (~ 90 °C) at room environmental conditions [73-75]. Other advantages of FM are process simplicity and yielding of acceptable PV parameters as previous studies have found [73].

Optical adhesives used included NOA 65 and NOA 71 that were obtained from Norland Products, Inc. and OEE from Ossila. NOA 65 is a clear, colorless, liquid photopolymer curable upon UV exposure (350-380 nm at 4.5 $mWcm^{-2}$). Its advantages are the elimination of premixing, drying, and heat curing operations; optical material bonding with bonding surfaces exposed to light; remarkable fast curing; and high flexibility and strain minimization through its adequate elasticity. Its applications include cold blocking, bonding plastic glass, and potting of lenses in metal mounts. Recently, they have been used in solar cell lamination due to their oxygen and moisture inhibition properties.

NOA 71 is an optically clear and UV-curable (315-400 nm at 3.5 $mWcm^{-2}$) liquid adhesive. Its advantages include optical clarity, fast curing times, and long-term stability over a wide temperature range, elimination of premixing, drying, and heat curing operations, provision of strong bond fiber- glass and glass surfaces. It can be typically used for lamination of touch screens, flat panel displays, holographic plates, and solar cells.

OEE is a colorless, UV-curable epoxy suitable for encapsulating organic PVs and OLEDs without polymer damage. This adhesive offers a robust against moisture and oxygen ingress alongside a glass coverslip to extend device lifetimes. Curing is achieved at 350 nm but can be considerably longer, up to 20 min, in the lab scale where lower intensities are often used. Table 2 summarizes the materials used for the fabrication of OSCs in this thesis including their solvents and providers.

Table 2. Materials and solvents used in this work for OSC fabrication.

Layer	Material abbreviation	Provider	Solvents
Anode	Glass/ITO	Delta Technologies	-
HTL	PEDOT:PSS	Heraeus-Clevios	Water
Active layer	P3HT	Thesis advisor's co-workers	CB
	PC70BM	Sigma Aldrich	
ETL	PFN	Sigma Aldrich	Methanol and acetic acid
Top electrode	FM	Rotometals	-
Encapsulation materials	NOA 65	Norland Products, Inc.	-
	NOA 71	Norland Products, Inc.	-
	OEE	Ossila	-

3.1.2. Device fabrication

OSCs were prepared in direct standard architecture and had the configuration ITO/PEDOT:PSS/P3HT:PC70BM/PFN/FM. The active layers used were the BHJ structure owing to its advantages earlier highlighted. The fabrication process involved sequential steps listed below.

- The glass/ITO substrates (1.5 cm by 1.5 cm) were cleaned using soap water, ethanol, and acetone by ultrasonication, 15 min for each solvent, dried in an oven at 80 ^{0}C for 15 min, and plasma-treated for another 15 min.
- PEDOT:PSS, used as HTL, was then spin-coated on the substrates at 5000 rpm for 1 min before annealing on a thermo-scientific hot plate at 120 ^{0}C for 15 min. the
- The active layer with donor (P3HT) and acceptor (PC70BM) blend was then spin-coated on the HTL at 2000 rpm for 1 min and annealed at 80 ^{0}C for 20 min. For the blend, 25 mg of donor and acceptor materials were mixed in the ratio of 1:1 by wt., dissolved in 1 ml of C_6H_5Cl, and stirred for 24 h before deposition.
- PFN, used as the ETL, was deposited on the active layer at 6000 rpm for 1 min and annealed at 80 ^{0}C for 10 min. For PFN solution, 1.0 mg was dissolved in 3.5 ml of methanol and 10 µl of acetic acid (0.143 vol %) was added before stirring for 24 h at room temperature.
- The FM was finally drop-coated at 90 ^{0}C on the PFN film with a delimited active area of 0.07 cm^2. Figure 15 exhibits the diagrammatic representation of the process.

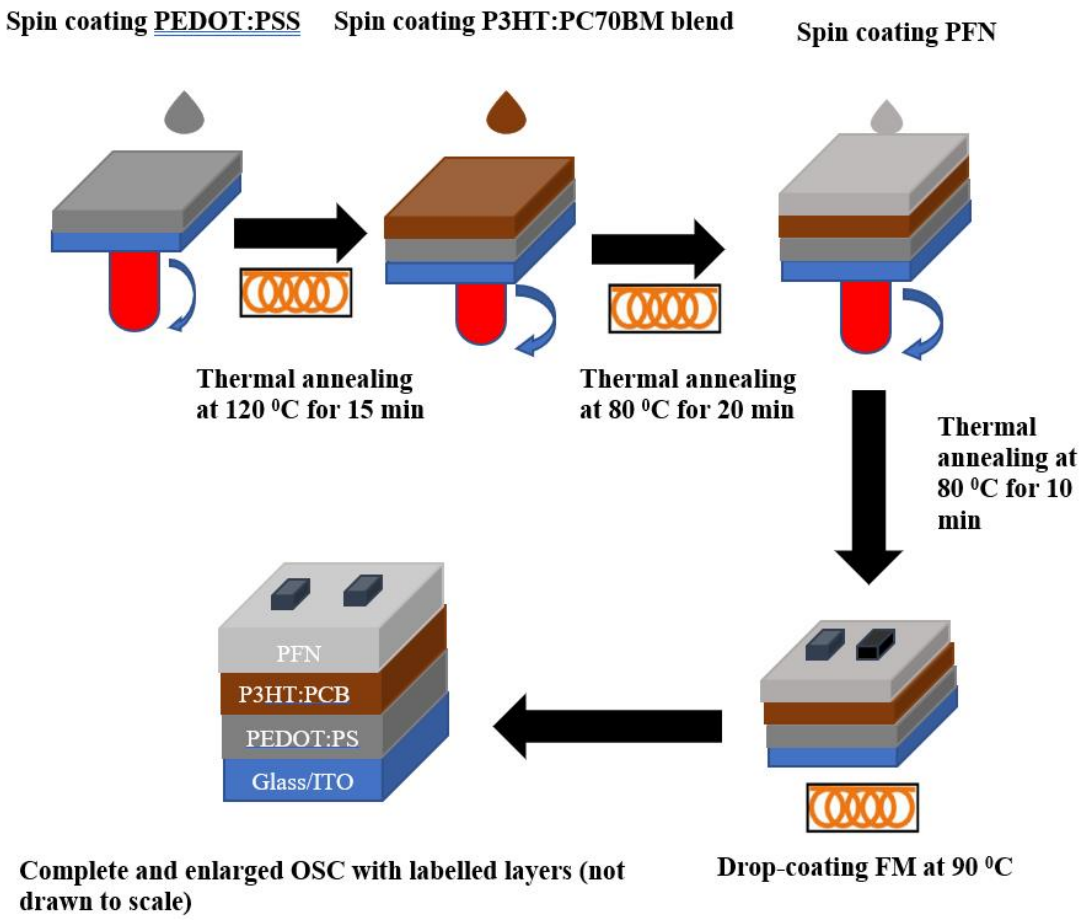

Figure 15. Schematic diagrammatic representation of organic solar cell fabrication procedure used in this work.

3.1.3. Device characterization

3.1.3.1. J-V characterization

After the fabrication of the OSC devices, *J-V* characterization was done using a solar simulator Sciencetech SS150 (AAA type). The light source was calibrated with AM1.5G spectra at 100 mWcm^{-2} by using an Oriel reference cell. Keithley 2450 source meter was used to measure the *J-V* curves, in which the cell parameters, J_{sc} and V_{oc}, were directly read from the vertical and horizontal axes, respectively (refer to Figure 3). These parameters then assisted in calculating the respective device PCEs as shown in Equation 1. All testing was conducted under an ambient atmosphere.

3.1.3.2. Device encapsulation and lifetime test

To perform an aging test for the devices, four of the fabricated best-performing cells were selected. While one of the PVs was left unencapsulated to act as the reference, the other three were encapsulated using the considered encapsulation materials (NOA 65, NOA 71, and OEE) in turn. This followed a four-step procedure as illustrated in Figure 16. A Pasteur pipette was initially utilized to drop a small quantity of one of the encapsulants on the substrate's/device's center and then spread to seal the device top and its edges. Next, a precleaned glass coverslip was placed on top of the substrate and carefully and slowly pressed down to enable adequate coating of the device by the epoxy. Then, the coverslip was gently pressed to remove any air bubbles that were present. For the effectiveness of the epoxy, the active area and metal cathode were fully covered by the adhesives. Finally, the substrates were transferred to a UV lamp area once all the coverslips were in position and spot cured for 5 min at 4.5 $mWcm^{-2}$ in case of OEE using Loctite® CL15 UV Curing Wand System. For NOA 65 and NOA 71 encapsulants, different UV curing times and intensities were used. Unlike the encapsulation using OEE, the curing times used for NOA 65 and NOA 71 were remarkably less (5 s) and at lower intensities of 4.5 $mWcm^{-2}$ and 3.5 $mWcm^{-2}$, respectively. After encapsulation using these materials, the *J-V* curves of both the encapsulated and the reference devices were measured once more using a Keithley 2450 source meter, and parameter changes from the initial values of each device were recorded before they (parameters) were monitored for 20 days under dark storage conditions to ensure slow degradation by preventing against harsh ambient conditions, such as high temperature at daytime, high solar illumination intensities, etc.

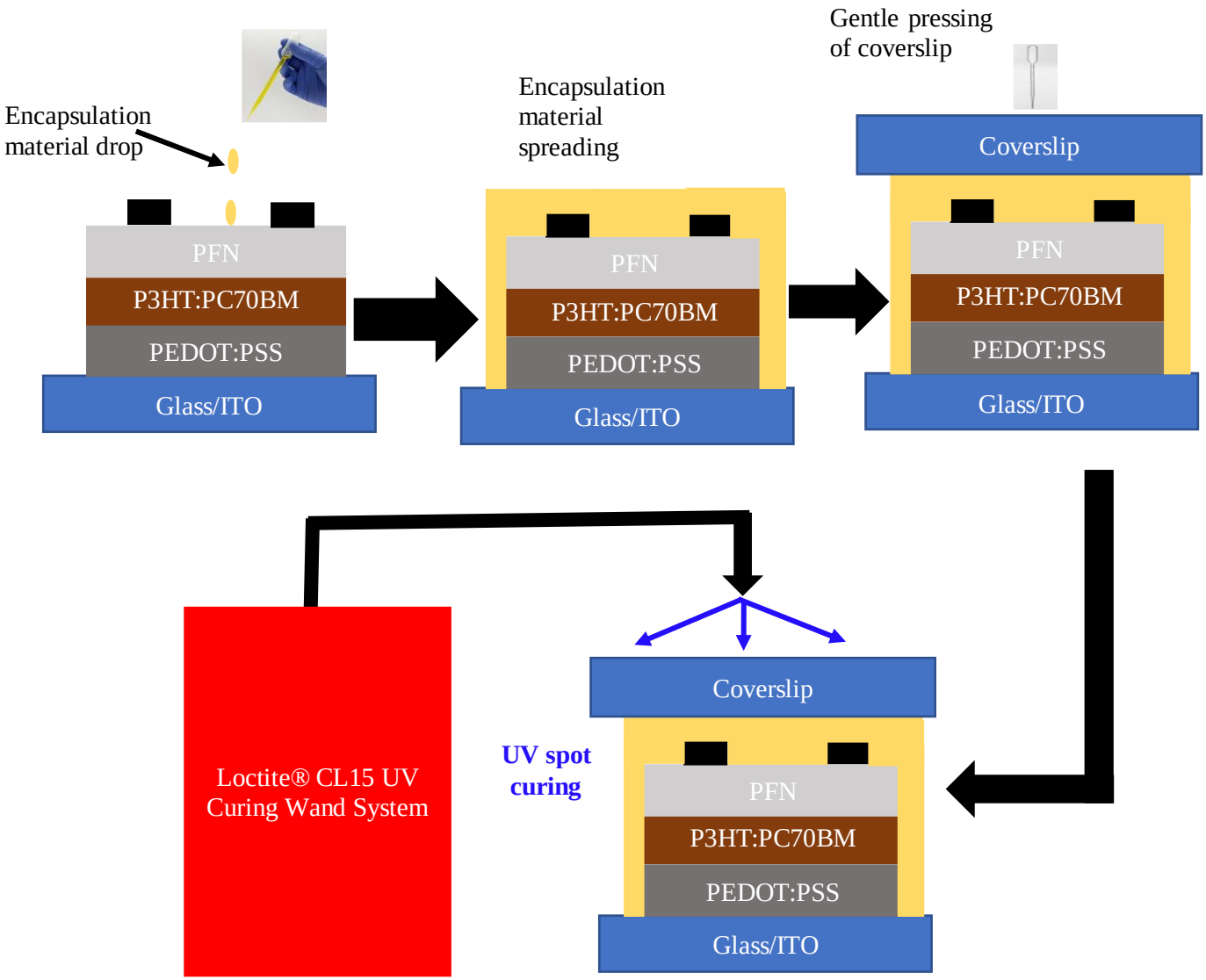

Figure 16. The encapsulation procedure for different adhesives used in this work.

3.1.3.3. Atomic force microscopy (AFM)

The AFM is a high-resolution, accurate, non-destructive, and high-resolution measurement technique used for the characterization of mechanical, optical, chemical, magnetic, electrical, and topographical properties of sample surfaces [76]. This microscopy technique uses silicon or silicon nitride with a sharp tip utilized for scanning layer surfaces. Upon approaching close to the film surface, the tip-film/substrate/sample forces cause the cantilever deflection, and a signal is achieved upon the reflection of the laser beam off the

cantilever. Thereafter, the cantilever deflection signal is rectified to a setpoint value. This is done by error signal minimization through a piezo controlled by feedback. Finally, the corrected signal is converted into high-resolution surface images. Different modes can be used to operate the AFM. They include contact and tapping modes. In general, the most commonly used imaging modes are the contact or non-contact/ "tapping" modes in which the cantilever oscillates or vibrates at some set frequency. In this thesis, the AFM was used to measure the topographical (morphological) characteristics roughness, and thickness of different device layers. An AFM Easyscan2 from Nanosurf with tapping mode was employed to carry out all the surface measurements roughness and morphology and thickness of different thin films, including HTL, OSC active layer, and ETL. Their thickness values were found to be 35 ± 5, 100 ± 8, and 7 ± 1 nm for HTL, active layer, and ETL, respectively.

3.2. Perovskite solar cells (PSCs)

3.2.1. Materials

Common materials used in PSC and OSC fabrication were acquired from the same suppliers. They included glass/ITO, PEDOT:PSS (Clevios PVP AI4083), PC70BM, and FM, CB, and all three encapsulants. On the other hand, materials that were specific to PSCs were purchased from various providers. Lead (II) chloride ($PbCl_2$) and Methylammonium iodide (MAI) were received from American Dye Source. All solvents, including Dimethylformamide (DMF), isopropyl alcohol (IPA), and CB, were acquired from Sigma Aldrich. Table 2 summarizes the materials used for the fabrication of PSCs in this thesis including their solvents and providers. Table 3 summarizes the materials used including their providers.

Table 3. Materials, solvents, and associated providers in this work.

Layer	Material abbreviation	Provider	Solvents
Anode	ITO/glass	Delta Technologies	-
HTL	PEDOT:PSS (4083)	Heraeus-Clevios	Water
Active	PbI_2	American Dye Source	DMF
	MAI	American Dye Source	IPA
ETL	PC70BM	Sigma Aldrich	CB
Top electrode	FM	Rotometals	-
Encapsulation materials	NOA 65	Norland Inc.	-
	NOA 71	Norland Inc.	-
	OEE	Ossila	-

3.2.2. Device fabrication

PSCs were fabricated in an inverted configuration, and the device arrangement was glass/ITO/PEDOT:PSS/$MAPbI_3$/PC70BM/FM. To start with, ITO/glass substrates were cut into sizes of 2 by 2 cm and were sequentially cleaned with soap water, ethanol, and acetone by ultrasonication, 15 min for each solvent. The substrates were then dried in an oven at 80 ˚C for 15 min and plasma treated for 15 min. Next, the PEDOT:PSS was spin-coated as HTL on the pre-cleaned and plasma-treated glass/ITO at 5000 rpm for 1 min and thermally treated at 120 ℃ for 15 min under ambient environmental conditions. The active layer perovskite ($MAPbI_3$) films were then processed on top of glass/ITO/PEDOT:PSS substrates by close-space sublimation (CSS) method in a vacuum oven at -0.8 bar (-600 mmHg), 130 ℃ for 1 h.

To carry out this procedure, the solutions containing the organic (MAI) and inorganic (PbI2) parts were first independently prepared and deposited, before the MAI was sublimated on the PbI_2 for conversion to $MAPbI_3$. The preparation of the solutions and hence their deposition involved a series of steps. First, PbI_2 solution of concentration 300 mg/ml was prepared by dissolving in DMF. It is important to remember that the precursor powder of PbI_2 was initially dried in a vacuum oven at 60 ºC for 24 h at -0.4 bar (-300 mmHg) before dissolving it. PbI_2 solution was then filtered out and spin-coated on the glass/ITO/PEDOT:PSS substrates at 3000 rpm for 1 min. Before its deposition, nevertheless, both the filtered PbI_2 and the substrates were pre-heated on the hot plate at 100 ^{0}C for 20 min. At the same time, glass substrates were used for MAI film deposition. The precleaned and plasma-treated substrates were placed on a hot plate at 60 ºC for 10 min and 200 µl of the MAI solution was uniformly drip-deposited and waited for the solvent to evaporate. Notably, the MAI solution of concentration 30 mg/ml was prepared by dissolving in IPA. Like PbI_2, MAI was simultaneously dried under the same conditions as PbI_2 before it was dissolved in IPA.

Subsequently, PCBM (35 mg/ml) in CB solution was spin-coated as the ETL onto the perovskite film at 1000 rpm for 30 s and heat-treated at 80 ^{0}C for 15 min. After delimiting the device active area to 0.07 cm^2 using tape, the FM was drop-coated on a hot plate at 90 ^{0}C on the delimited area. Figure 17 illustrates the sequential two-step CSS method used for PSC preparation**.**

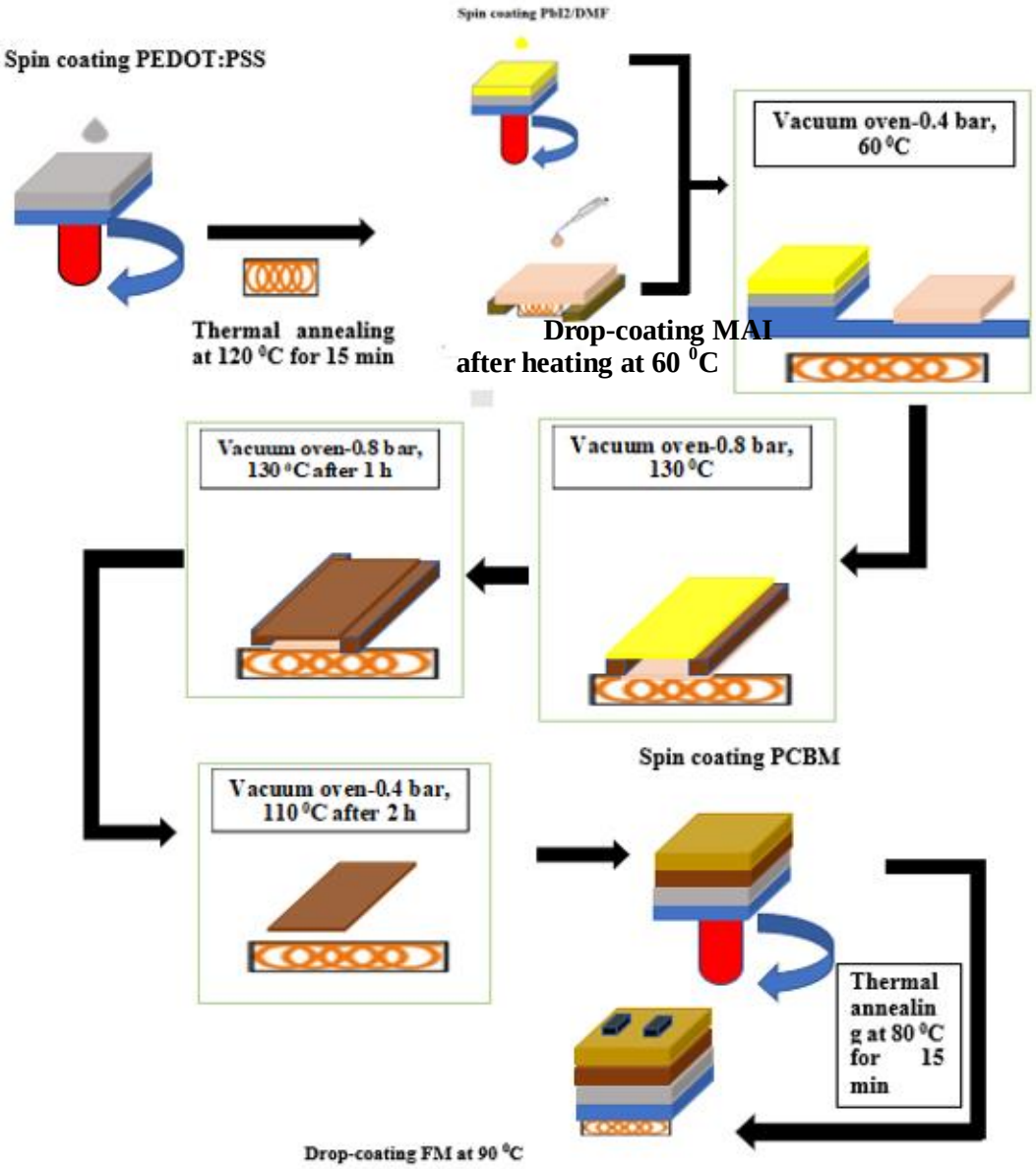

Figure 17. Schematic diagrammatic representation of PSC fabrication procedure using sequential two-step CSS and spin coating methods.

3.2.3. Device characterization

For PSC device characterization, the steps described for *J-V* measurements, lifetime tests, and AFM characterization were followed. The perovskite active layer morphological

properties were determined. For PSCs, the thickness range values of HTL, perovskite layer, and ETL were 38-42, 385-405, and 97-100 nm, respectively.

3.3. UV-visible spectroscopy

The UV/Vis spectral absorption and transmission curves for the three encapsulation materials, including OEE, NOA 65, and NOA 71, were determined using the Perkin Elmer spectrophotometer model Lambda 900. This instrument was used to measure absorption/transmission intensity as a function of light source wavelength. A Pasteur pipette was used to drop small quantities of the encapsulants on the center of precleaned glass substrates. Then, each material was carefully spread gently and uniformly on the substrates for the adhesive to sufficiently coat on the substrate surfaces. The spreading eliminated air bubbles. Once the spreading was complete, the glass substrates were UV cured in succession according to the datasheets of each material. The optical performance of the cured adhesives on the substrates was then determined using a spectrophotometer in the wavelength range 300-800 nm.

4. Analysis of results

In this chapter, we extensively and comprehensively discuss the results of the *J-V* characterization, encapsulation, and lifetime/aging results of the fabricated OSCs and PSCs prepared using the techniques described in the methodology section. The influence of different encapsulation materials on the stability of OSCs and PSCs was particularly observed by electrically characterizing them and studying the variation of their key performance parameters, including PCE, J_{sc}, V_{oc}, and FF with time. The morphological characterization was represented due to the important role it plays in device performance. In addition, the encapsulation materials were characterized through UV-Vis spectroscopy to examine their optical transparency performance and hence their suitability for utilization in device protection. Ultimately, this chapter discusses the results to deduce the possible reasons for the variation of performance of the encapsulants and suggests the best adhesive from among the ones considered in this work.

4.1. Organic Solar Cells (OSCs)

In this subsection, an analysis of the morphological properties of the fabricated cell layers was carried out. Additionally, encapsulated and reference cells' stability was monitored for 20 days.

4.1.1. Device performance

Organic solar cells were prepared using the ITO/PEDOT:PSS/P3HT:PC70BM/PFN/FM architecture as shown in Figure 18. After the preparation, *J-V* characterization was used to measure all the excitonic cells to help in selecting the best-performing but similar in terms of parameters, including PCE, J_{sc}, V_{oc}, and

FF. Such devices were encapsulated and stored in dark conditions. For lifetime tests, the parameters were taken out, measured, and/or calculated after two days for 20 days.

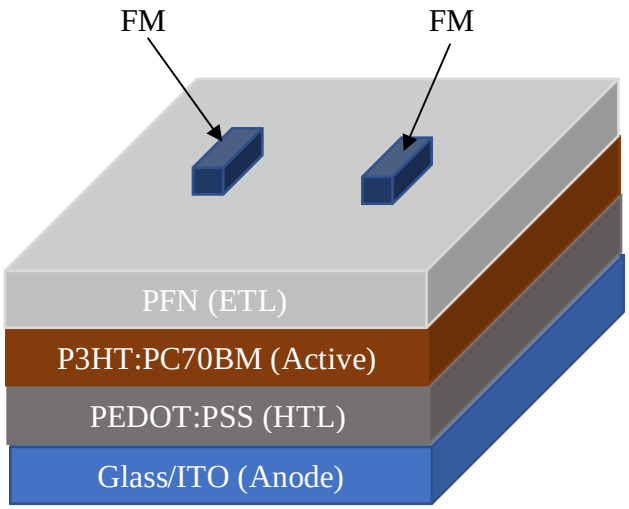

Figure 18. The 3-D view of a standard OSC fabricated in this thesis is shown constituting various layers.

Figure 19 represents the *J-V* curves for the pristine cells that were eventually obtained immediately after completion of the improved fabrication process. As can be seen from the figure, the curves obtained showed good and reasonable repeatability. Initially, in some sets of cells, the device reproducibility was a key concern, as the curves varied significantly and led to the achievement of less efficient cells (0.8%). These large variations resulted from poor morphology and deposition of films on relatively large area ITO substrates (2.5 by 2.5 cm) that created nonuniformity or inhomogeneity of cell films. Accordingly, to ensure the cells were repeatable and their performance nontrivially improved, the quality of the films was improved by carefully depositing thin-film layers on smaller area glass/ITO substrates (1.5 by 1.5 cm) and spin coating with greater care, thus improving morphology and leading to reproducible and more efficient devices. In particular, to control and optimize the morphology and achieve high-efficiency solar cells, our work focused on post-treatment conditions and blend composition, which has been reported to have a strong influence on the

OSC performance based on donor (P3HT) and acceptor (PCBM) materials [77, 78]. For active layer blend composition, a 1:1 weight ratio of P3HT and PCBM was used to yield the more efficient devices in our study. This ratio contradicts some studies that recently obtained efficient devices with a weight ratio of 1:0.8 for the two material blends for the active layer [79].

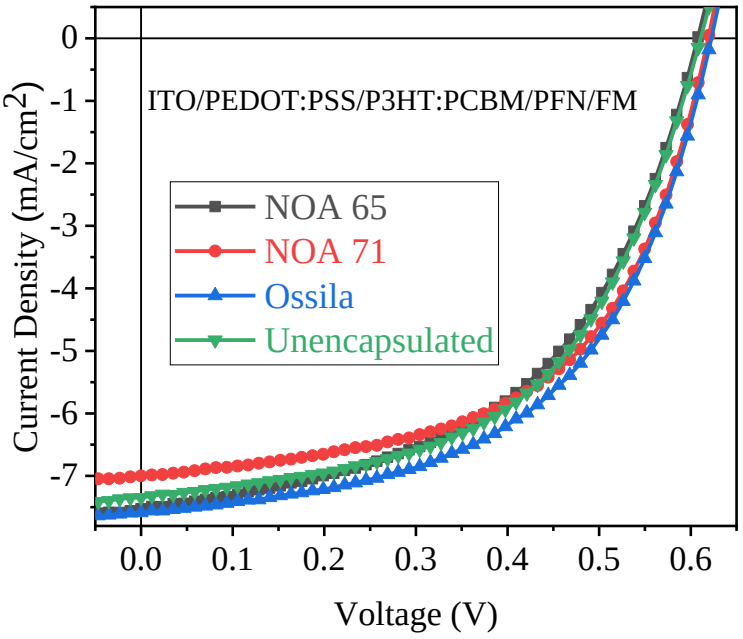

Figure 19. The J-V curves of freshly prepared OSCs and encapsulated with different adhesives for aging test for days.

Table 4 shows the distribution of four pristine OSC performance parameters derived from the curves. Observably, the current density values in the curves are negative as a sign convention to show that current is flowing out from the anode (generating energy). Thus, the negative values in the table were disregarded and absolute values were used instead for further analysis in this thesis. Whereas the range PCE values recorded for the improved cells with greater reproducibility was 2.43-2.650%. J_{sc}, V_{oc}, and FF range values were 7.35-7.62 $mAcm^{-2}$, 0.61-0.62 V, and 0.53-0.58, respectively. Although the J_{sc} and V_{oc} values agree with

some studies [79], they were generally low. For instance, J_{sc} for all the devices was low despite using a high absorption coefficient, BHJ active layer material (P3HT) [28], and allowing the D-A materials to mix for 24 h, and these low values may have been due to the recombination of generated excitons before dissociation and free charge carriers at the acceptor-ETL and acceptor-HTL interfaces causing low collection efficiency [79]. On the other hand, low V_{oc} may have been due to the presence of nonohmic contacts at the electrode/ETL interface and poor D-A blend morphology [79]. The low J_{sc} and V_{oc} were, therefore, the cause of low FF observed in our results, which also signified higher R_s and low R_{sh} as described earlier under the single-diode junction model [14]. As shown in Eq. 2, these parameters strongly and directly affect device performance, and conspicuously led to lower efficiencies than what the literature has reported thus far using optimized P3HT:PCBM active layer (3-5%) [80].

Table 4. The PV parameters of OSCs used in this thesis.

Device	***VOC* (V)**	***JSC* (mA/cm^2)**	***Pmax* (mW/cm^2)**	***FF***	***PCE* (%)**
NOA 65	0.61	-7.52	2.45	0.53	2.43
NOA 71	0.62	-7.01	2.51	0.58	2.52
Ossila	0.62	-7.62	2.63	0.56	2.65
Unencapsulated	0.61	-7.35	2.55	0.57	2.56

4.1.2. Morphology

As already highlighted in 4.1.1., surface roughness and thickness are some of the key factors that also influence device performance, and as such, it was necessary to analyze them following optimization through active layer blend composition and thermal annealing of

different layers. Analyses of these film aspects were especially crucial. The AFM images of the three layers with 10 by 10 μm scanning size are shown in Figure 20. Surface analysis revealed surface roughness of approximately 3, 2, and 1 nm for the HTL, active, and ETL, respectively. These roughness values are similar to those of other research studies that have previously been reported [78, 79]. From the fabricated films shown in the figure, it is observed that the images have better defined granular morphology which can only be linked to the optimized conditions implemented during the fabrication procedure such as post-treatment as well as spin coating speed and time. These favorable morphological structures possibly led to reduced charge trapping and fostered charge extraction and transport [81].

For the thickness, the estimation was done by making cuts on the glass/ITO surfaces containing each of the deposited films. Since these thicknesses are estimates, three measurements were taken at different cut locations of the samples for every layer, and the average value of each measure was determined. Our thickness measures for the layers were found to be 35 ± 5, 100 ± 8, and 7 ± 1 nm for HTL, active layer, and ETL, respectively. The active layer thickness is remarkably within the range of 65-266 nm reported in the literature as necessary for efficient light-harvesting and charge generation [79]. Just like roughness, the average thickness values are similar to what other studies have found.

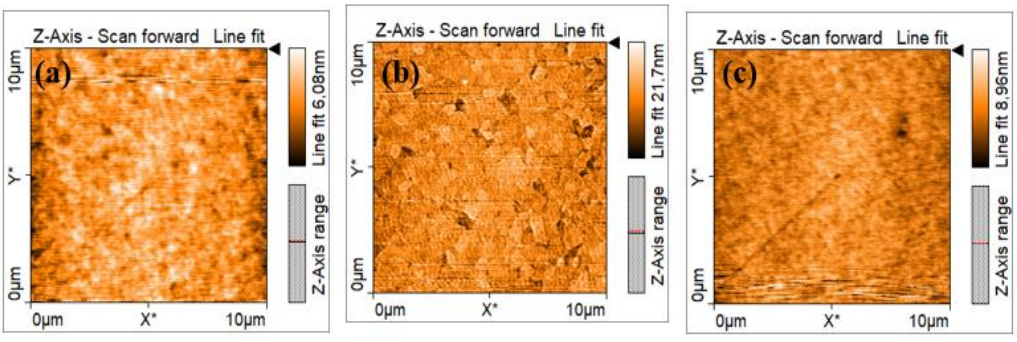

Figure 20. The AFM images of various OSC layers (a) HTL, (b), the active layer, and (c) ETL.

4.1.3. Stability test results

Figure 21 illustrates the cross-sectional view of an encapsulated OSC used in this thesis. The encapsulation material covered both the top and edges of the solar cell. As previously mentioned, one of the OSCs was left unencapsulated to act as a reference device. After the encapsulation procedure, the devices interestingly did not significantly lose their performance, possibly because of the fast-curing process that did not give time for environmental factors to cause consequential deterioration and low intensities that did not break polymer carbon bonds to impact performance. The encapsulated cells and the non-encapsulated reference devices were stored in the dark for 20 days and the variation of the four parameters, PCE, J_{sc}, V_{oc}, and FF, were monitored with time, with measures taken every 2 days. It is important to note that these tests were conducted in three sets of cells, and it was observed that the stability performance trend of the encapsulation materials was similar. Accordingly, our study selected one of the sets for further analysis and reporting.

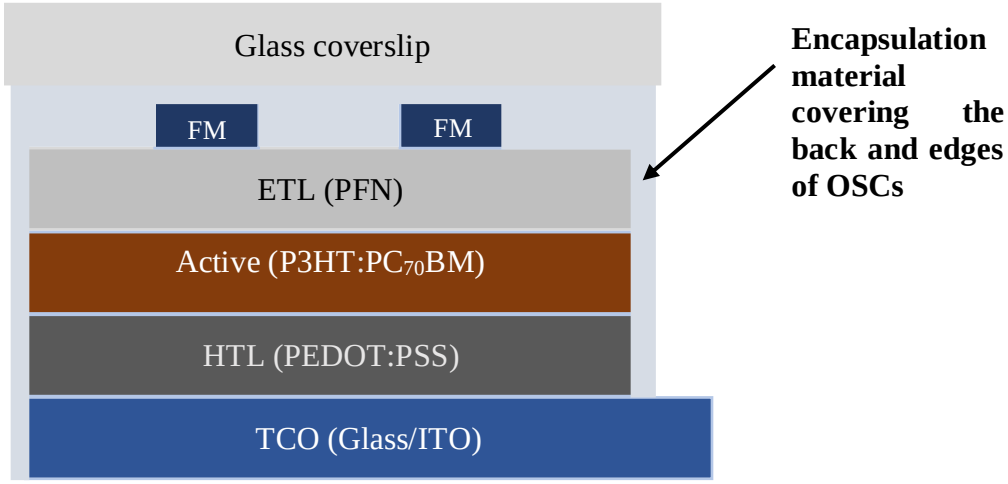

Figure 21. Cross-sectional view of fully encapsulated OSC device using the blanket method.

Figure 22 shows the variation of absolute PCEs with time. It can be seen that in all the cell devices, the PCEs dropped and did so at different rates throughout the aging period.

The rates were notably dependent on the encapsulant that was considered for each case. It was observed that OEE provided significantly greater stability by maintaining a better cell performance compared to both the NOA adhesives and the reference, as it decreased least rapidly and retained 92.5% of its original efficiency. Interestingly, OEE was closely followed by NOA 71 and NOA 65 respectively, which retained efficiencies of 91.3% and 87.0%, respectively. As expected, the reference OSC recorded the least performance of all, retaining only 38.0% of the original efficiency value during the aging test. An important point to note from Figure 17 is that better-performing adhesives also had retained their original performance for longer times before they began to deteriorate. As such, we can immediately conclude OEE was most effective in safeguarding cell devices from the ingress of water and oxygen, which are the main degrading causing factors in OSCs.

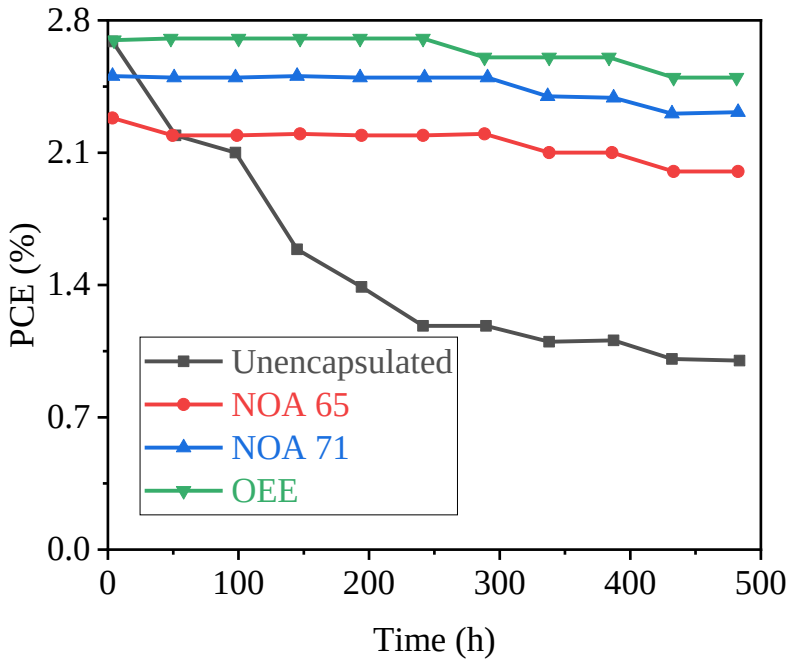

Figure 22. The variation of PCE vs time of encapsulated and unencapsulated OSCs.

Similarly, Figure 23 exhibits that J_{sc} decreased with time over the same period, with the OEE and NOA 71 registering the better performance over NOA 65 by each retaining 95% of the initial value. NOA 65-encapsulated device retained 94% of their initial value, while the reference cell retained only 66%, indicating the highest rate of degradation. Of course, it is evident that compared to PCE values, which is considered the most important and determinant parameter, relatively small decrements were witnessed in J_{sc} values. As seen in these curves, the negative sign convention in the *J-V* curves was omitted and absolute values were used in J_{sc} to demonstrate the decreasing or degrading property of this parameter with time.

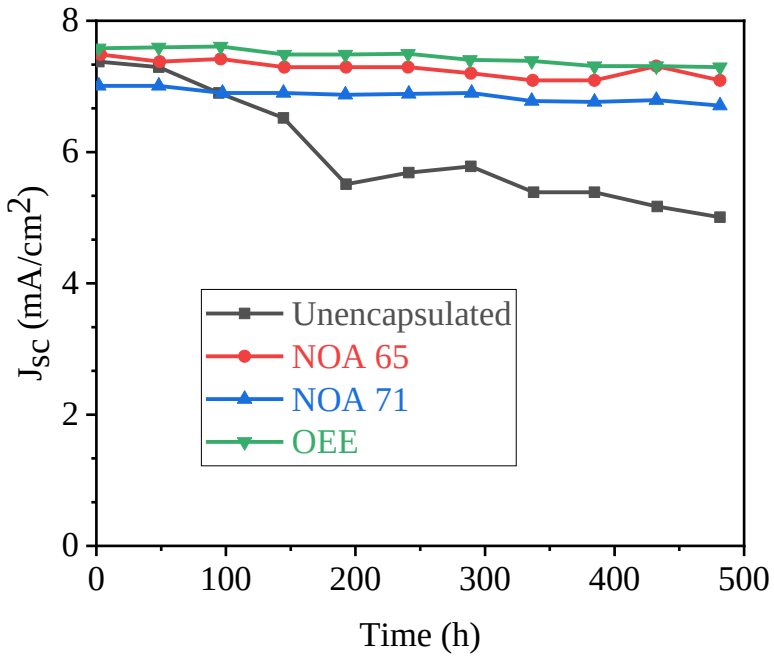

Figure 23. The variation of Jsc vs time of encapsulated and unencapsulated OSCs.

Contrary to the PCEs and J_{sc} with easily noticeable deterioration rates, little to no changes were observed in the other parameters, namely V_{oc} and FF. Over the testing period, as depicted in Figure 24, the V_{oc} of most of the devices slightly decreased irrespective of

whether the device was encapsulated or not. This slight reduction made it challenging to reliably use this parameter in gauging the impact of encapsulation materials on devices. Nevertheless, the small variations were still visible, as close observations demonstrated that the rate of decrease differed depending on the encapsulation material, with the reference device starting to drop first followed by those of NOA 65 and NOA 71, and finally OEE after 48, 192, 288, and 384 h, respectively. Therefore, while the ultimate reductions were small for all adhesives, the differing rates exhibited that encapsulants generally ascertained voltage stability compared to the non-encapsulated reference device. This retention further depended on the material, with OEE retaining the initial value of V_{oc} longer than the rest.

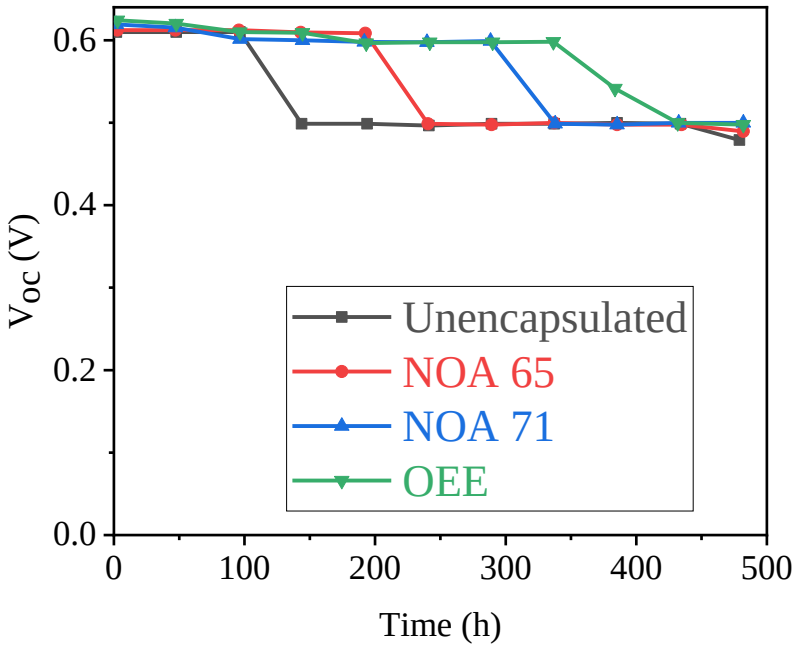

Figure 24. Variation of V_{oc} vs time of encapsulated and unencapsulated OSCs.

Figure 25 shows how FF changed during the lifetime test. While some OSCs showed a gradual loss of FF, others oscillated and instead had their FF values increase. More particularly, the encapsulated cells showed a steady but slow loss in their FF, although this

was often less radical and the changes were only slightly noticeable, occurring more pronouncedly when the cells were already exhibiting tremendously reduced PCEs at 336 h for NOA 71 and OEE. The percentage reductions registered by these adhesives, respectively, were 13.8% and 10.7%. Interestingly, the FF value of the NOA 65 encapsulated device oscillated between and increased and somewhat stabilized at a higher value unlike other devices (increased from 0.53 to 0.60 or increased by 13.2%). This contradicts previous studies that have found that whereas FF might sometimes improve, it stabilizes and slowly starts to decrease with time [82], due to reduced charge extraction from the degrading active layer [83]. This improvement was despite the overall PCE decrease determined in NOA 65, which might have been apparently due to more dramatic declines of other parameters, such as J_{sc} and V_{oc}. Although the results provided by the encapsulated device curves might be inconclusive on how FF varies with time, it can be seen from the unencapsulated device that if the test could be conducted for more time, reductions may potentially be steadier and more reliably observed, as it lost 33.3% of the initial value after 20 days.

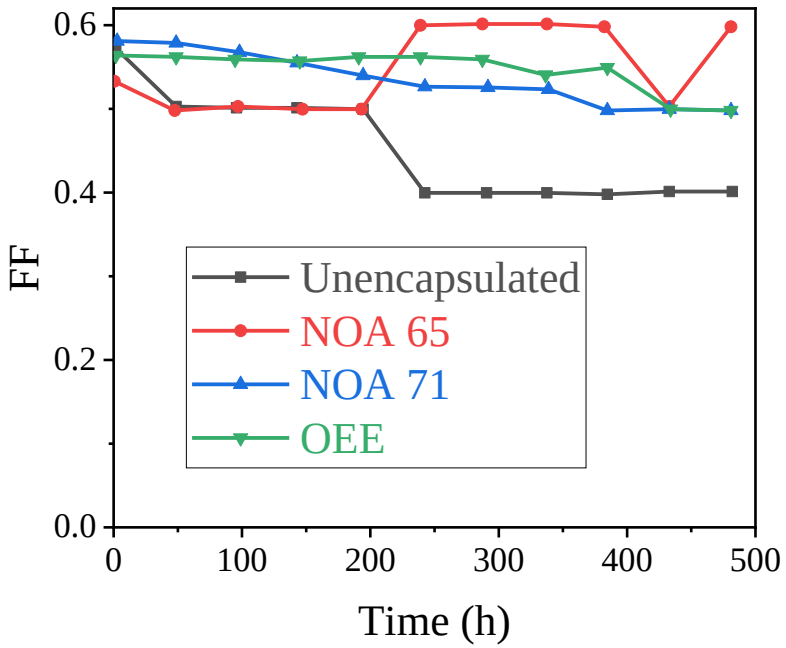

Figure 25. The variation of FF against the time of encapsulated and unencapsulated OSCs.

The *J-V* characterization of the results obtained with the encapsulated and reference OSCs demonstrated the effect that encapsulation materials have on improving stability. The encapsulated excitonic devices particularly showed greater stability than the unencapsulated OSC, with OEE being the best followed by NOA 71 then NOA 65, and finally the unencapsulated one. Good PCE performance retention in OEE has been found in other studies as well. Using epoxy encapsulant under damp-heat conditions, Sapkota, et al. found that OSCs encapsulated between glass-glass retained over 90% of their initial device performance after more than 1800 h; more remarkably, another device set retained a similar performance after over 12,000 h under continuous one-sun irradiation [84]. Our results are also consistent with previous findings involving NOAs that have shown NOA 71 to be a better encapsulation material than NOA 65 [13].

Equally observable is that the PCE and J_{sc} were more reliable in evaluating the effect of encapsulation materials on device degradation, as they recorded clearer declines. These device parameters were better compared to V_{oc} and FF, whose results showed unclear outcomes, although some conclusions could be derived from them, especially if the lifetime test was conducted for an extended time in the range of 1000 h and over [84]. Overall, OEE is the best material among the encapsulants used in this thesis then NOA 71 and finally NOA 65.

4.2. Perovskite Solar Cells (PSCs)

As with the previous subsection, here we also analyze the device performance of the fabricated PSCs, the morphological properties of their different layers, and more importantly, their stability or aging after 20 days following encapsulation with the three adhesives.

4.2.1. Device performance

PSCs with an inverted structure was manufactured. Figure 26 shows the fabricated device with glass/ITO/PEDOT:PSS/$MAPbI_3$ perovskite/PC70BM/FM architecture. The inverted architecture was especially considered because of its low-temperature processing, relatively high throughput, easy fabrication, and cost-effectiveness for upscaling [20, 50].

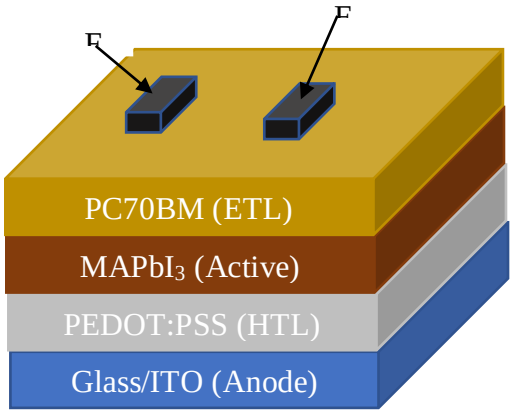

Figure 26. The 3-D view of an inverted PSC fabricated and used in this thesis.

Figure 27 shows the *J-V* curves of the freshly manufactured devices obtained. To try and achieve better device performance, our efforts were directed at controlling a wide array of parameters, including the vacuum oven temperature as well as thermal treatment time and temperature to achieve efficient perovskites with greater homogeneity, reproducibility, and crystallinity. However, realizing all these was an extremely challenging task given the sensitivity of these solar cells to ambient factors. As the figure reveals, cells with high reproducibility were achieved, and this was done by controlling the morphology and film quality by using suitable annealing conditions to ensure film homogeneity [73]. The reproducibility was also realized by carefully and uniformly spread-coating the MAI solution on pre-cleaned and pre-treated glass substrates for the $MAPbI_3$ perovskite films to be homogenously formed.

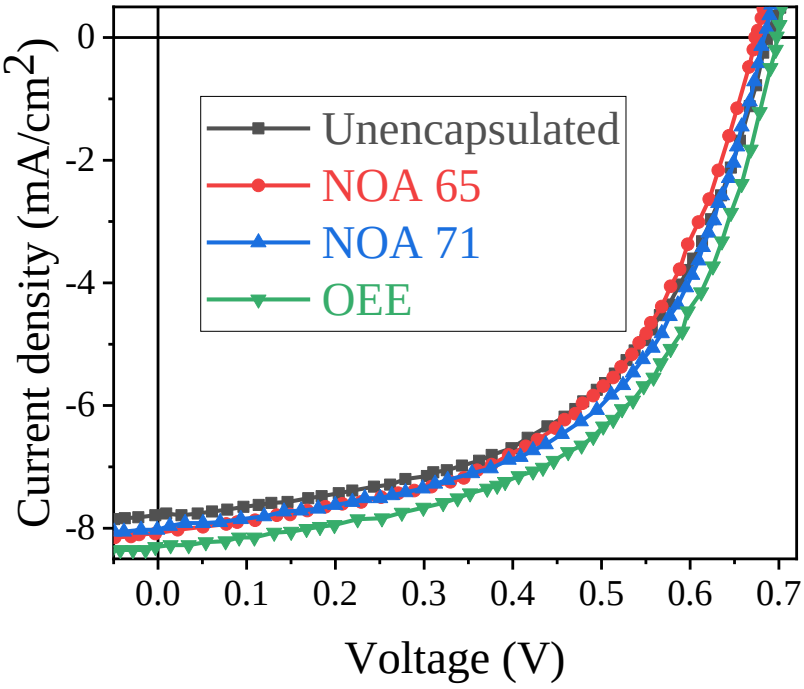

Figure 27. The J-V curves of freshly prepared PSCs show their performance.

Table 5 exhibits the parameters of the manufactured PSCs. The PCEs ranged between 2.84% and 3.21%. On the other hand, J_{sc}, V_{oc}, and FF values ranged from 7.76-8.30 mA/cm^2, 0.67-0.70 V, and 0.53-0.56, respectively. Like in OSCs, low PCEs were obtained in PSCs, as the CSS has previously yielded better PCEs, up to 10% [85]. This could be as a result of internal factors caused by the low J_{sc}, V_{oc}, and FF, with direct influence on efficiency. For low Jsc, the reason could be that pinholes and defects may have been present in the perovskite layer, leading to increased recombination and loss of photo-generated carriers at the grain boundaries. In addition, the poor interface morphology could be another reason. These two factors have been found to result in ineffective collection and transport of photo-generated carriers [21, 85]. Although charge collection efficiency can be improved through defect passivation involving the addition of a new layer, such as 2,5-thiophenedicarboxylic acid ligand, between the perovskite and the charge transport layers (CTLs) [85], our work did not use these materials; thus, future studies could consider it. Our highest Voc value was 0.70 V, which is inconsistent with what some studies have found (1.20 V). Similar reasons cited for OSCs, such as poor interface layer or nonohmic contact, could the caused these lower values. Combined with low FF, it was without a doubt that our PCEs would be low.

The low PCEs may have as well been caused externally by "excess" atmospheric moisture and oxygen. The fact that our devices were fabricated under high ambient relative humidity (RH) conditions (48-54%) may have contributed to low efficiencies, as high RH has been shown to adversely influence perovskite film crystal growth and performance, especially when it is above 30% [86]. Even though a dehumidifier was used to reduce the levels of humidity in the lab, they did not reduce significantly since the dehumidifier was not in good working conditions. Possibly, preparing the perovskite films in a glove box, where conditions are controlled might have potentially produced more efficient devices. The

temperatures in the vacuum oven were maintained in the range of 127 ℃-134 ℃ to obviate the decomposition of the temperature-sensitive perovskites. This is consistent with Soo, et al. who suggested temperatures below 150 ℃ to avoid degradation of device layers and performance degradation [87].

Table 5. Summary of freshly prepared PSC devices showing the device parameters.

Device	***VOC* (V)**	***JSC* (mA/cm^2)**	**P_{max} (mW/cm^2)**	***FF***	***PCE* (%)**
Unencapsulated	0.69	−7.76	-2.85	0.53	2.84
NOA 65	0.67	−8.03	-2.85	0.53	2.85
NOA 71	0.68	−7.97	-2.99	0.56	3.03
OEE	0.70	−8.30	-3.18	0.55	3.20

4.2.2. Morphology

In PSCs, morphology engineering plays an invaluable role in their performance just as in OSCs. The morphological properties that were analyzed were surface roughness and thickness, although other components like grain size and crystallinity are crucial as well. The AFM was employed to inspect surface roughness and thickness. Figure 28 provides the extracted image scans of different films. The images demonstrate films with well-defined grain boundaries, especially the $MAPbI_3$ perovskite and ETL layers. The measured thickness of HTL, $MaPbI_3$ perovskite, and ETL ranged between 38-42, 385-405, and 97-100 nm, respectively. On the other hand, the surface roughness for these layers was measured to be 3,

19, and 5 nm, respectively. These layer thickness and roughness values demonstrated were in line with several previous studies that have provided similar ranges for these layers [88, 89].

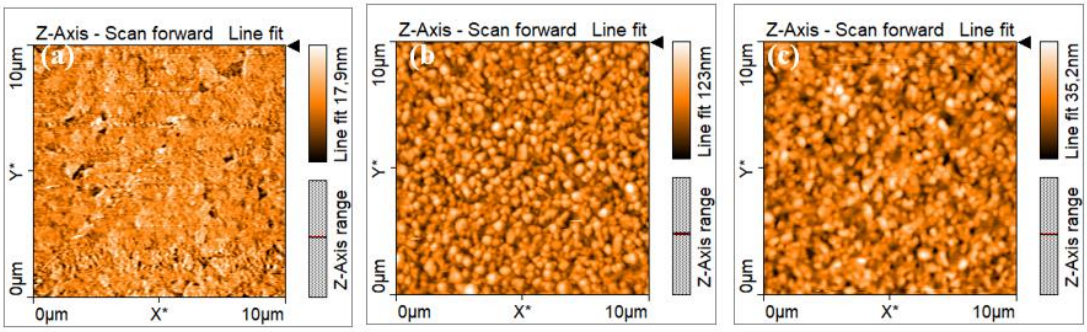

Figure 28. AFM images of (a) HTL fabricated by simple spin coating, (b) MAPbI3 perovskite processed by sequential two-step close-space sublimation, and (c) HTL achieved by spin coating techniques.

Figure 29 indicates the sample photographs of PbI_2 films that were taken after CSS in the vacuum oven. It can be seen that the resulting film images had uniform yellow color distribution without white spots, signifying homogeneity. This was achieved at the PbI_2 film spin coating stage, where PbI_2-DMF solution and glass/ITO/PEDOT:PSS substrates were both thermally pretreated separately at 100 ℃ for 20 min before spin-coating the former on the latter, as these conditions enhance fast crystallization resulting from induced temperature gradients caused by the spin coater [88, 89]. This minimizes boundaries and increases the average grain size within the perovskites to reduce recombination of the photogenerated charges [89]. Other annealing conditions have been demonstrated to produce irregular and white spot poor-quality films. Therefore, ensuring homogeneity of perovskite film during fabrication by thermal pre-treatment was one of the crucial methods for improved morphology.

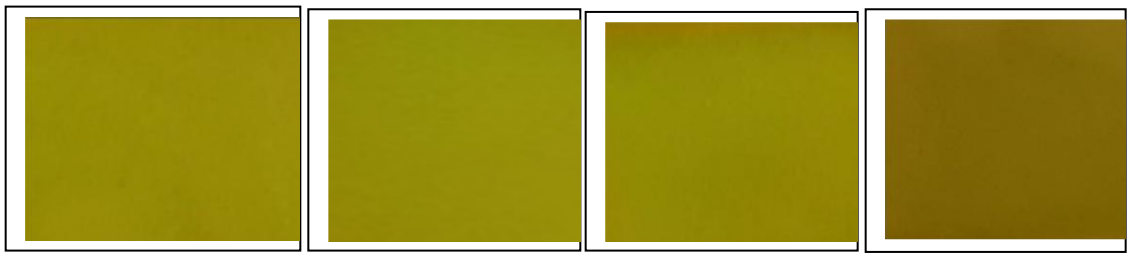

Figure 29. Sample photographs of high-quality and homogenous bright yellow PbI2 films obtained suitable pre-treatment of substrates and PbI2-DMF solution at 100 °C for 20 min.

For this thesis, one device was left unencapsulated to act as the control/reference cell, while the other three devices were encapsulated with NOA 65, NOA 71, and OEE, to examine the effect and compare the performance of these adhesives on solar cell stability and lifetime. Figure 30 shows the cross-section of an encapsulated PSC with blanket encapsulation material covering the top and edges of the device. Similar to OSCs, three sets of solar cells were tested, and a similar stability performance trend was observed across the sets and encapsulants. As such, this thesis work chose one of the sets for further analysis and reporting.

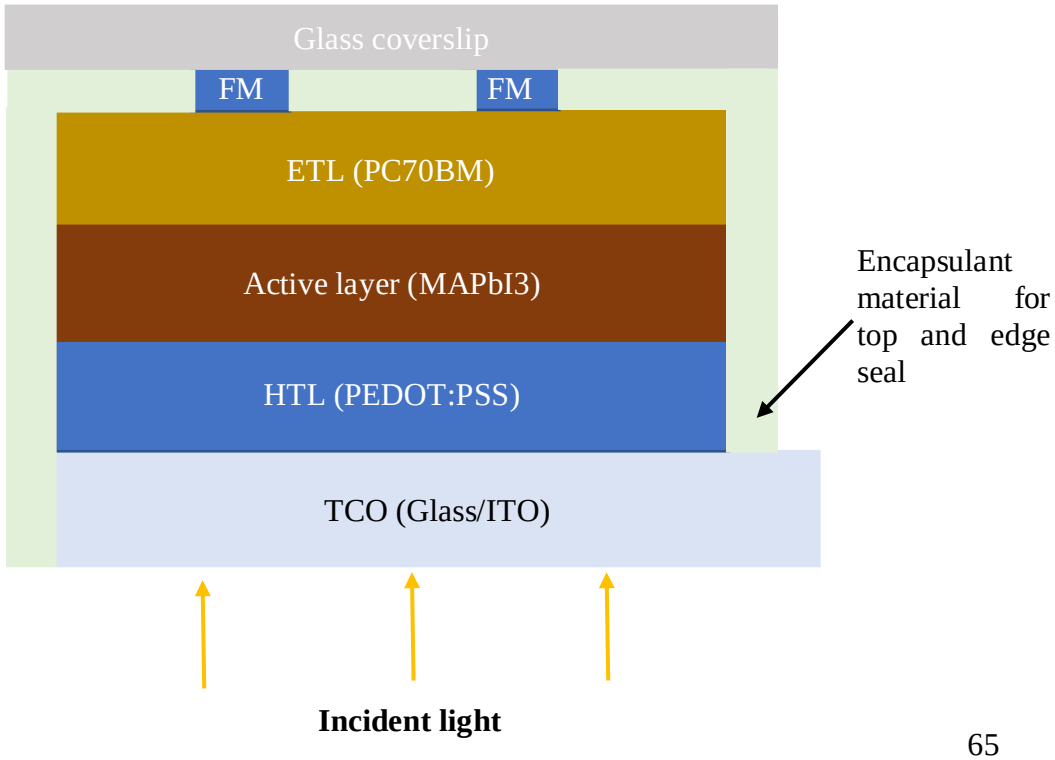

Figure 30. The cross-sectional view of an encapsulated inverted PSC device. The encapsulant covers both the top and edges of devices.

Table 6 presents the performance parameters just after the encapsulation and curing at UV wavelengths described in 3.2.3. It was observed that both the encapsulated and reference device parameters, including PCEs, J_{sc}, V_{oc}, and FF, reduced after the encapsulation procedure. This was not surprising considering the PSCs were exposed to the ambient conditions during the encapsulation process after the initial *J-V* characterization, potentially causing performance loss. Indeed, the reduction, especially PCE, was more pronounced in encapsulated cells (1.4%, 4.3%, and 10.1% for NOA 65, NOA 71, and OEE compared to the 0.35% for unencapsulated) that were UV irradiated. The device encapsulated using OEE had the highest reduction probably because of the higher UV irradiation intensity that was used for its curing (4 $mWcm^{-2}$ for 5 min). UV curing during encapsulation procedure has generally been reported to trigger damage to cells and lead to losses. Although the reductions may have also been caused by the encapsulants due to lack of excellent optical transmission efficiency that leads to the obstruction of light/photons from reaching the perovskite layers and ultimately decreasing the conversion efficiency, this was not the case as the incident light hit the PSCs from the glass/ITO or anode direction (see Figure 30), and therefore did not affect the absorption by the active layers.

Table 6. Device parameters immediately after the encapsulation with different encapsulants.

Device	***VOC* (V)**	***JSC* (mA/cm^2)**	**P_{max} (mW/cm^2)**	***FF***	***PCE* (%)**
Unencapsulated	0.69	−7.74	-2.84	0.53	2.83

NOA 65	0.63	−7.97	-2.79	0.56	2.81
NOA 71	0.65	−7.82	-2.90	0.57	2.90
OEE	0.67	−8.25	-3.10	0.55	2.87

After the encapsulation and consequently *J-V* characterization, the PSCs were stored in the dark and various performance parameters were monitored for 20 days. Ultimately, the variability of different performance parameters against time was plotted.

Figure 31 shows the variation of PCE measurements vs time. The findings reveal that the PCEs for all the devices deteriorated regardless of the encapsulation state of the device. However, this took place at significantly varying rates, with a higher loss rate occurring in the unencapsulated device than its encapsulated counterparts. While the unencapsulated device retained a PCE fraction of 33.5%, its encapsulated counterparts retained much higher values as expected. In particular, the PCS protected using NOA 65 and NOA 71 retained efficiency fractions of 77.6% and 80%, the one safeguarded using OEE retained an efficiency fraction of 85.5% after 20 days. The results audibly demonstrate that encapsulation plays an important role in PCE retention. Most importantly, they show that the epoxy offers better efficiency retention compared to other adhesives that were considered in this work and are therefore more effective in device stability maintenance.

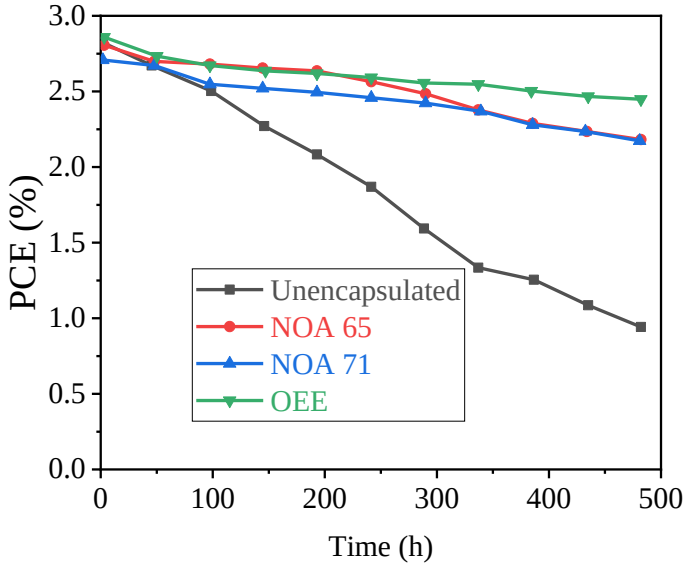

Figure 31. The variation of PCE vs time of encapsulated and unencapsulated PSCs.

The rate of change of J_{sc} vs time is another important parameter that this study monitored, and a similar observation to that seen in PCEs, i.e., reduction with time, was made as shown in Figure 32. However, the rate of reduction differed significantly depending on whether there was encapsulation or not. Even among the encapsulated PSCs, the rate of change varied observably. As anticipated, the greatest reduction rate occurred in the non-encapsulated cell which fell to 3.97 from 7.74 mA/cm^2, recording a retention J_{sc} fraction of 51.3%. On the other hand, encapsulated devices retained *Jsc* fractions of 79.5%, 85.1%, and 86.5% for NOA 65, NOA 71, and OEE, respectively. Similarly, OEE registered the best performance over its counterparts that were considered.

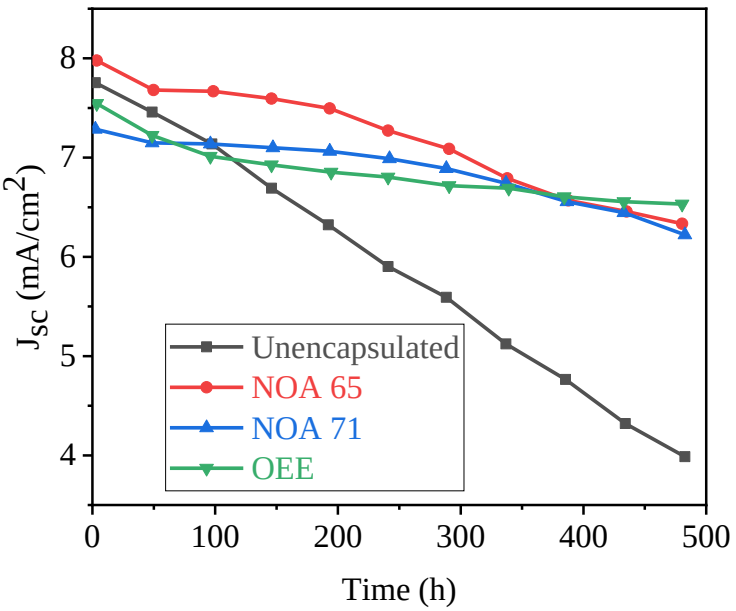

Figure 32. The variation of Jsc vs time of encapsulated and unencapsulated PSCs.

For the variation of V_{oc} shown in Figure 33, the highest reduction was likewise observed in the non-encapsulated device, which lost 34.8% of its original value and retained 65.2%. By contrast, little to no reductions in V_{oc} were recorded in encapsulated cells. While NOA 65 and NOA 71 retained 97.0% and 95.5% of their initial values, respectively, the epoxy was able to equally retain the highest, 98.6%. Therefore, unlike the previously discussed parameters of PCE and J_{sc}, V_{oc} decreases less rapidly and should thus be monitored over an extended time to yield considerably more revealing and comparable results as suggested in OSC lifetime tests. However, the difference if the device is not encapsulated is evident but findings somewhat point to the epoxy as the best-performing adhesive.

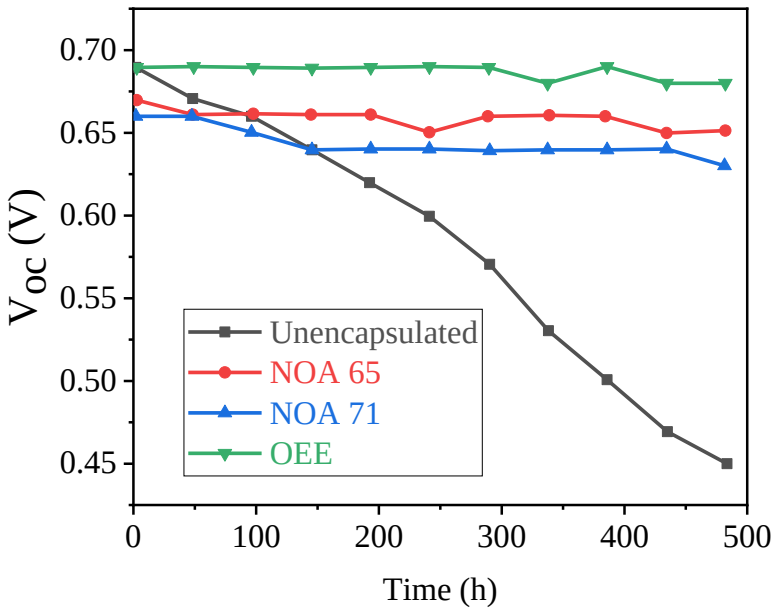

Figure 33. The variation of Voc vs time of encapsulated and unencapsulated PSCs for 20 days.

Figure 34 indicates how the FF parameter varied with time, and like other parameters, it depicts a downward trend, with encapsulation demonstrating its protection ability of devices here as well. While the non-encapsulated PCS retained 62.3% of its initial value, the reference PSCs had minimal to no change in their FF values. Specifically, NOA 65 and NOA 71 retained 92.3% and 98.2%, respectively, the epoxy did not record any change after the 20 days, implying it retained 100.0% of its initial performance. Accordingly, OEE outperformed the NOAs, with NOA 71 coming second followed by NOA 65.

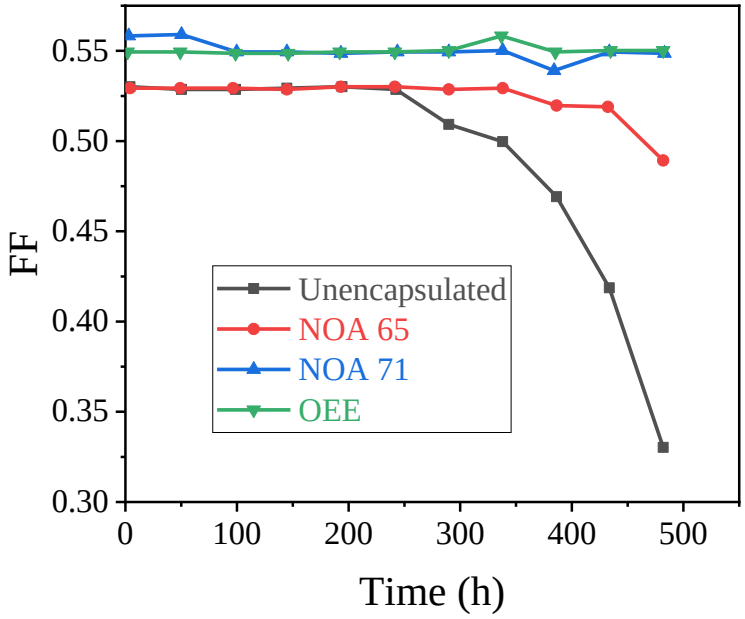

Figure 34. Variation of FF vs time of encapsulated and unencapsulated PSCs for 20 days.

In summary, the findings from PSC curves reveal that like in OSCs, OEE offers the best barrier of PSC protection against moisture and oxygen, followed closely by NOA 71, while NOA 65 comes third. In contrast, the reference unencapsulated PSC was the least and comes distant fourth, as it lost most of its performance due to the absence of encapsulation during the lifetime test. Although both the performance parameters recorded a general reduction in their original values, it was clear that PCE and J_{sc}, to some extent, provided more reliable results in the short-time assessment of the effect of encapsulation on PV stability.

4.3. UV-Vis spectroscopy

Figures 35 and 36 show the UV-Vis spectroscopy spectra of the encapsulants used to characterize them for optical performance. Figure 35 illustrates that the transmission of the considered encapsulants in this work. The results showed that NOA 65 and NOA 71 transmit from 400-800 nm at ~95%, while the epoxy does so from 450-800 at ~90%. Thus, the NOAs were better optical transmitters than the epoxy. However, all the materials have the unique

property to block UV light completely from 300-400, which makes them suitable for PV applications where UV blocking is crucial, yet transmission is required in the visible wavelengths.

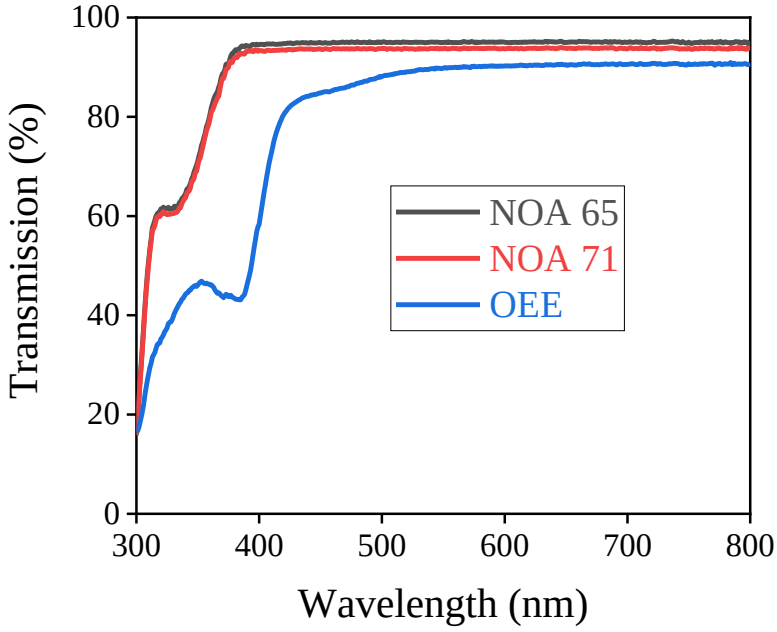

Figure 35. The UV-Vis spectroscopy (transmission spectra) was measured using a spectrophotometer. The tests were performed on both NOA 65, NOA 71, and Ossila epoxy resin films in region UV-Vis-NIR.

Figure 36 presents complementary curves of transmission, depicting the absorption spectra of these adhesives used in this thesis. As can be seen, NOAs have lower absorption in the visible wavelengths compared to OEE with relatively higher absorption. NOAs start to absorb at 380 nm, whereas OEE starts at 500 nm, which demonstrates the poor optical performance of OEE than NOAs with inevitably greater clarity. Despite this less optical transparency, lifetime tests in both OSCs and PSCs showed OEE as the most effective in protecting devices against environmental factors. This, therefore, suggests there could be many other factors that could be impacting the performance of these materials as will be discussed in the later section.

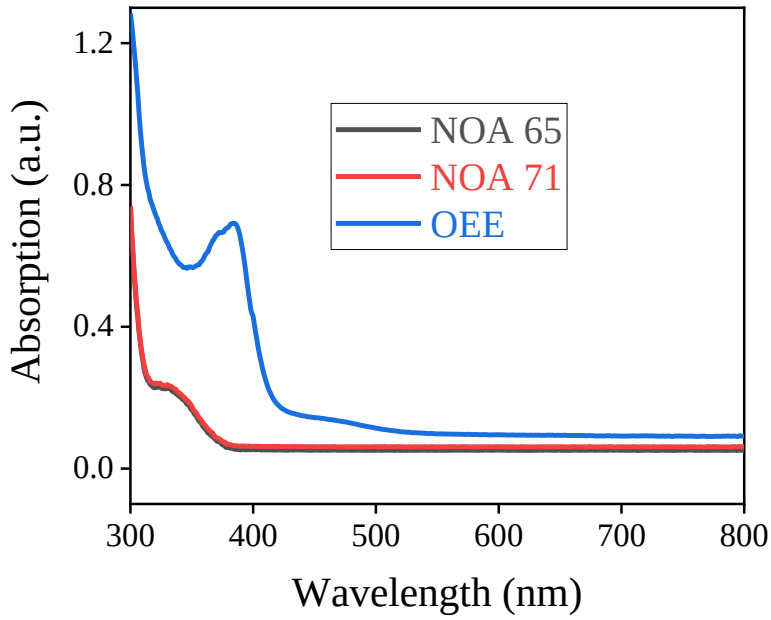

Figure 36. The UV-Vis spectroscopy (absorption spectra) was measured using a spectrophotometer. The tests were performed on both NOA 65, NOA 71, and Ossila epoxy resin films in region UV-Vis-NIR.

4.4. Comparative discussions

The results obtained from OSCs and PSCs show interesting points that are worth being discussed. These devices are different in terms of charge generation and occasionally in processing methods. Regarding their fabrication, it was established that preparing PSCs using the sequential two-step CSS technique is more complex and time-consuming than OSCs, which are fabricated mainly through simple spin coating. We expected PSCs to achieve better device efficiency performance because of optimized fabrication conditions and nature of charge generation; absorption causes the direct and efficient generation of free charges in a single step rather than excitons that experience considerable energy losses through their migration and dissociation [45, 46]. However, we did not achieve this good efficiency for reasons cited earlier under PSC device performance. Most notably, we

observed that PSCs are more sensitive to environmental factors of oxygen and moisture, as the reference PSCs degraded more rapidly (retained 33.5%) than the reference OSCs that retained PCE of 38.0% at the end of the aging period.

All the encapsulated devices aged; however, the degradation rates were more drastic in PSCs than in OSCs. This was because PSCs are more sensitive to the ambient conditions compared to the excitonic devices. The performance decline in encapsulated OSCs and PSCs may have been caused by many reasons. First, it appears that although the device active areas were safeguarded to a great extent by top electrodes and encapsulants, they were insufficient to completely circumvent deterioration [68], as the low WVTR and OTR of the encapsulants still permitted oxygen and moisture to enter through the device layers into the photoactive layers and reach sufficient levels to initiate degradation processes described earlier. Secondly, the materials could be made up of reactive and harmful chemical elements that interact with various materials within the device stack to degrade cell performance. Wong et al. have recently tested the reactivity of OEE's film, where they found that the resin appreciably reduced perovskite film absorbance and cited the undesirable chemical reactions between $MAPbI_3$ and OEE as the probable reason for the dwindling perovskite performance [90]. Few studies have used NOAs to investigate this phenomenon, and have suggested the possibility of chemical reactants that hamper performance [66, 84]. To improve the encapsulation effect, attain high-performance encapsulation barriers, and prevent possible chemical reactions between the active and polymeric resins, multilayer encapsulation barrier structures incorporating encapsulants and interlayer materials such as a solution-processable polymer interlayer (polyvinylpyrrolidone (PVP)) and Poly (methyl methacrylate) (PMMA) can be used [90].

Interestingly, in both OSCs and PSCs, OEE registered the best performance followed by NOA 71 and finally NOA 65, which we instantly argue could be the result of lower WVTR and OTR in OEE than in the other materials. The similarity in performance of these materials was not surprising, as many recent studies have suggested that, unlike their inorganic counterparts, several materials used as HTLs, ETLs, electrodes, etc., in OSCs can also be incorporated in PSCs and still perform excellently [21]. Accordingly, we anticipated that encapsulation materials capable of providing better performance in OSCs could equally perform better in PSCs.

Our UV-Vis transmission results showed better optical transparency performance of NOAs (>95%) than OEE (>90%) and would, therefore, expectedly be more suited to providing better encapsulation performance. However, WVTR, OTR, and transmission/absorption are just but a few parameters that influence encapsulation performance from among many others, such as adhesion, modulus, elongation at failure, refractive index, tensile stress, etc. [71]. This explains OEE's better performance than the NOAs despite its poorer optical performance. Its chemical make-up ensures that it optimizes and trades off all these variables to offer the best barrier performance. For instance, other than its possibly lower WVTR and OTR already highlighted, this material contains a tackifier resin which promotes adhesion and stability performance of OEE as well as creates a trade-off between optical performance and adhesion. As such, while the tackifier may potentially reduce the light transmission and increase absorption, the increased adhesion compensates for the reduced optical performance and plays a vital role in improving encapsulation/mechanical strength and hence long-term stability. In addition, OEE's lower index of refraction (~1.5) [89] compared to NOA 65 (1.52) and NOA 71 (1.56) [92] minimizes optical losses in form of reflection and absorption. Indeed, a recent report found

that epoxies, such as OEE, can be invaluable in Pb toxicity reduction in PSCs by preventing its leakage by a higher factor (375) than other conventional UV-curable resins such as NOAs [93]. In sum, a combination of variables, namely excellent adhesion to glass, outstanding optical properties even after curing, superb electrical insulation, improved Pb leakage prevention, higher temperature resistance, as well as extremely low WVTR and OTR, ascertains that OEE offers better performance than most other adhesives.

However, these enormous stability benefits of the OEE come at a cost. This is because while the epoxy is best in terms of stability, it considerably costs more ($95.30 for a 10 ml bottle) than both NOA 65 ($23.28 for 30 ml) and NOA 71 ($22.11 for 30 ml) [91, 92]. Therefore, including it in device processing might lead to increased and high overall device production costs, potentially making OSCs and PSCs economically less competitive than the existing PV technologies in the market. Consequently, all the three key elements of the golden triangle, namely efficiency, lifetime or stability, and cost, may not be optimized. Nevertheless, it should be emphasized that these costs are for small quantities and at the research level. For future scaling and commercialization, prices could be significantly reduced. This warrants a more extensive study that elaborately examines the golden triangle components to assess the suitability of these materials to meet all the three factors, while also ensuring device competitiveness with the existing energy sources when devices are ultimately upscaled.

5. Conclusions and future work

This chapter provides a summary of lifetime testing comparison results of OSCs and PSCs. It also briefly states the findings obtained by this research project and suggests recommendations for future studies.

5.1. Conclusions

In this thesis, stable standard organic solar cells (OSCs) and inverted perovskite solar cells (PSCs) were fabricated. Three different UV-curable encapsulation materials, including Norland adhesive 65 (NOA 65), Norland adhesive 71 (NOA 71), and Ossila encapsulation epoxy (OEE), were purposely used to inhibit external factors, especially moisture and oxygen, causing device degradation. The aim was to compare the encapsulants and identify the most effective among them in terms of barrier protection. To that end, we designed, encapsulated, and rated respective performance parameters of different sets of OSCs and PSCs. The parameters considered were power conversion efficiency (PCE), short-circuit current density (J_{sc}), open-circuit voltage (V_{oc}), and fill factor (FF), which were monitored for 20 days under dark storage conditions. Although we immediately conclude that encapsulation depends on barrier encapsulant performance ability, especially water vapor transmission rate (WVTR) and oxygen transmission rate (OTR), other parameters, such as transmission/absorption, modulus, tensile strength, refractive index, etc., have a vital role in the overall performance. The main findings from the analysis include:

- For OSCs processed by spin coating technique, the maximum PCE was 2.70%, although this PCE was lower than what has been reported in the literature. For PSCs processed by sequential two-step close-space (CSS) fabrication method, the

maximum efficiency was 3.20%. Again, this was lower than the efficiencies in the literature that have found up to 10%. The low device PCEs could be due to charge carrier recombination, poor interface morphology, and harsh ambient fabrication conditions.

- The device layer morphological properties, especially surface roughness and film thicknesses, were consistent with what has been reported in the literature thus far. For OSCs, the surface roughness was found as 3, 2, and 1 nm for the hole transport layer (HTL), P3HT:PC70BM active layer, and electron transport layer (ETL), respectively. For PSCs, the surface roughness was measured to be 3, 19, and 5 nm, for HTL, $MAPbI_3$ perovskite layer, and ETL, respectively. The grain boundaries were also well-defined for all the devices.
- Encapsulation results revealed that under the same environmental conditions, OEE offers the best barrier protection against moisture and oxygen for both OSCs (retains 92.5% of initial PCE) and PSCs (retained 85.5%) despite its least UV-Vis transmission/absorption among the three adhesives. It is followed closely by NOA 71 (retained 91.3% and 80% for OSCs and PSCs, respectively), while NOA 65 (retained 87.0% and 77.6% for OSCs and PSCs, respectively) comes third. The lowest performance was found in the reference or unencapsulated cells. Therefore, OEE's excellent performance was due to the trade-off between different parameters, including WVTR, OTR, transmission/absorption, adhesion, refractive index, modulus, tensile strength, etc., which influence the overall material encapsulation performance. Although the costlier nature of this adhesive makes it inconclusive to say it is the best encapsulant cost-effectively, as economic viability might be a great

concern, this research is only in the lab-scale and costs could potentially decrease in upscale production.

- Our findings reveal that the PCE and J_{sc} were the most reliable performance indicators in providing accurate results on the effect of encapsulation in devices over a short time of 20 days and can be used to better predict the effect of encapsulants on device performance when lifetime tests under such short spans. For V_{oc} and FF, however, the rate of decrease is more gradual and not easily visible for a few weeks. This was particularly the case in OSCs.

5.2. Future work

Future studies could complement the results of this work in different ways. First, works could try to fabricate devices with relatively higher efficiency in the glove box, minimal relative humidity conditions, and improved morphology. Second, the best encapsulant that optimizes all the three components of the golden triangle, namely efficiency, stability, and costs, may be inconclusive. Thus, future upscale studies could try to establish the most cost-effective and best barrier protection adhesive to attain competitiveness with alternative photovoltaics (PVs) in the market. Our results, however, point to the OEE as the best encapsulant in terms of stability performance in the lab research. Consequently, more extensive upscale research should be conducted to establish the encapsulation material that optimizes all the three components in the golden triangle before full commercialization. In addition, multilayer encapsulation could be included to enhance their performance effectiveness. Besides, the research could identify the exact adhesive chemical constituents that might lead to performance deterioration.

Third, our current study included NOA 65, NOA 71, and OEE. While the findings were promising, future studies could be more robust and incorporate more wide-ranging encapsulation materials. They could also experimentally quantify and analyze how innumerable parameters, namely thickness, WVTR, OTR, optical performance, modulus, refractive index, volume resistivity, etc., impact the encapsulation performance of each material. Finally, the research could also be conducted over an extended time with these varieties of adhesives to better establish how all the parameters, including V_{oc} and FF, vary with time so that they can help with how encapsulation impacts them.

6. References

[1] R. B. Jackson, C. Le Quéré, R. M. Andrew, J. G. Canadell, J. I. Korsbakken, Z. Liu, G. P. Peters, and B. Zheng, "Global energy growth is outpacing decarbonization," *Environ. Res. Lett.*, vol. 13, no. 12, p. 120401, 2018.

[2] "U.S. Energy Information Administration (EIA) – Release." [Online]. Available: https://www.eia.gov/pressroom/releases/press487.php. [Accessed: 03-Nov-2021].

[3] A. R. Douvan, "The G20 peer review of fossil fuel subsidies," in *Environmental Fiscal Challenges for Cities and Transport*, Edward Elgar Publishing, 2019, pp. 241–256.

[4] R. Ramirez, "Why ending our dependence on fossil fuels is so challenging," *CNN*, CNN, 04-Oct-2021.

[5] J. Carriquiry, C. Treinen-Crespo, J. Villaescusa, A. Pearson, and L. Barbara, "The impact of global warming on the upwellings and primary productivity at the southern limb of the California Current, Baja California, Mexico," 2020.

[6] Y. Quilcaille, T. Gasser, P. Ciais, F. Lecocq, G. Janssens-Maenhout, and S. Mohr, "Uncertainty in projected climate change arising from uncertain fossil-fuel emission factors," *Environ. Res. Lett.*, vol. 13, no. 4, p. 044017, 2018.

[7] D. Gielen, F. Boshell, D. Saygin, M. D. Bazilian, N. Wagner, and R. Gorini, "The role of renewable energy in the global energy transformation," *Energy Strat. Rev.*, vol. 24, pp. 38–50, 2019.

[8] C. Zhang, C. Shen, Q. Yang, S. Wei, G. Lv, and C. Sun, "An investigation on the attenuation effect of air pollution on regional solar radiation," *norland* .

[9] F. Creutzig, P. Agoston, J. C. Goldschmidt, G. Luderer, G. Nemet, and R. C. Pietzcker, "The underestimated potential of solar energy to mitigate climate change," *Nat. Energy*, vol. 2, no. 9, p. 17140, 2017.

[10] B. C. Brusso, "A brief history of the energy conversion of light [history]," *IEEE Ind. Appl. Mag.*, vol. 25, no. 4, pp. 8–13, 2019.

[11] "Solar PV – Renewables 2020 – Analysis - IEA," *Iea.org*. [Online]. Available: https://www.iea.org/reports/renewables-2020/solar-pv. [Accessed: 03-Nov-2021].

[12] E. Kabir, P. Kumar, S. Kumar, A. A. Adelodun, and K.-H. Kim, "Solar energy: Potential and future prospects," *Renew. Sustain. Energy Rev.*, vol. 82, pp. 894–900, 2018.

[13] L.-M. García-Encina, "Encapsulation of organic solar cells with polymeric resins, their PV performance and lifetime," Centro de Investigaciones en Optica, León, Guanajuato, México, 2016.

[14] Z. Tang, J. Wang, A. Melianas, Y. Wu, R. Kroon, W. Li, W. Ma, M. R. Andersson, Z. Ma, W. Cai, and W. Tress, "Relating open-circuit voltage losses to the active layer morphology and contact selectivity in organic solar cells," *J. Mater. Chem. A Mater. Energy Sustain.*, vol. 6, no. 26, pp. 12574–12581, 2018.

[15] M. M. Rhaman and M. A. Matin, "Organic Solar Cells: Historical developments and challenges," in *2015 International Conference on Advances in Electrical Engineering (ICAEE)*, 2015.

[16] S. E. Shaheen, C. J. Brabec, N. S. Sariciftci, F. Padinger, T. Fromherz, and J. C. Hummelen, *2. 5% efficient organic plastic solar cells," Appl. Phys. Lett.*, vol. 78, no. 6, pp. 841–843, 2001.

[17] Z. He, C. Zhong, S. Su, M. Xu, H. Wu, and Y. Cao, "Enhanced power-conversion efficiency in polymer solar cells using an inverted device structure," *Nat. Photonics*, vol. 6, no. 9, pp. 591–595, 2012.

[18] Y. Cui, Y. Xu, H. Yao, P. Bi, L. Hong, J. Zhang, J. Qin, J. Ren, and Z. Chen, "Single-junction organic photovoltaic cell with 19% efficiency," *Adv. Mater.*, vol. 33, no. 41, p. e2102420, 2021.

[19] Q. Liu, Y. Jiang, K. Jin, J. Qin, J. Xu, W. Li, J. Xiong, J. Liu, Z. Xiao, K. Sun, and S. Yang, "18% Efficiency organic solar cells," *Sci. Bull. (Beijing)*, vol. 65, no. 4, pp. 272–275, 2020.

[20] Y. Sun, G. C. Welch, W. L. Leong, C. J. Takacs, G. C. Bazan, and A. J. Heeger, "Solution-processed small-molecule solar cells with 6.7% efficiency," *Nat. Mater.*, vol. 11, no. 1, pp. 44–48, 2011.

[21] N. Marinova, S. Valero, and J. L. Delgado, "Organic and perovskite solar cells: Working principles, materials, and interfaces," *J. Colloid Interface Sci.*, vol. 488, pp. 373–389, 2017.

[22] S. Rafique, S. M. Abdullah, K. Sulaiman, and M. Iwamoto, "Fundamentals of bulk heterojunction organic solar cells: An overview of stability/degradation issues and strategies for improvement," *Renew. Sustain. Energy Rev.*, vol. 84, pp. 43–53, 2018.

[23] F. Laquai, D. Andrienko, C. Deibel, and D. Neher, "Charge carrier generation, recombination, and extraction in polymer–fullerene bulk heterojunction organic solar cells," in *Elementary Processes in Organic Photovoltaics*, Cham: Springer International Publishing, 2017, pp. 267–291.

[24] G. Sauvé and R. Fernando, “Beyond fullerenes: Designing alternative molecular electron acceptors for solution-processable bulk heterojunction organic photovoltaics,” *J. Phys. Chem. Lett.*, vol. 6, no. 18, pp. 3770–3780, 2015.

[25] L. E. Sousa, V. Coropceanu, D. A. da Silva Filho, and G. Sini, “On the physical origins of charge separation at donor-acceptor interfaces in organic solar cells: Energy bending versus energy disorder,” *Adv. Theory Simul.*, vol. 3, no. 4, p. 1900230, 2020.

[26] A. Gusain, R. M. Faria, and P. B. Miranda, “Polymer solar cells-interfacial processes related to performance issues,” *Front. Chem.*, vol. 7, p. 61, 2019.

[27] J. Zhang, Y. Zhang, J. Fang, K. Lu, Z. Wang, W. Ma, and Z. Wei, “Conjugated polymer-small molecule alloy leads to high efficient ternary organic solar cells,” *J. Am. Chem. Soc.*, vol. 137, no. 25, pp. 8176–8183, 2015.

[28] Y. Cui, P. Zhu, X. Liao, and Y. Chen, “Recent advances of computational chemistry in organic solar cell research,” *J. Mater. Chem. C Mater. Opt. Electron. Devices*, vol. 8, no. 45, pp. 15920–15939, 2020.

[29] S. K. Shah, “Fabrication of bulk heterojunction organic solar cells with different configurations using electrospray,” *Nano Express*, vol. 1, no. 2, p. 020037, 2020.

[30] Y. Wang, B. Wu, Z. Wu, Z. Lan, Y. Li, M. Zhang, and F. Zhu, “Origin of efficient inverted nonfullerene organic solar cells: Enhancement of charge extraction and suppression of bimolecular recombination enabled by augmented internal electric field,” *J. Phys. Chem. Lett.*, vol. 8, no. 21, pp. 5264–5271, 2017.

[31] T. M. Clarke and J. R. Durrant, “Charge photogeneration in organic solar cells,” *Chem. Rev.*, vol. 110, no. 11, pp. 6736–6767, 2010.

[32] M. Shafiey Dehaj, M. Ahmadi, and S. Ghazanfarpour, “Inverted bulk heterojunction organic solar cells using optimization of active layer deposition via controlling of doctor blade parameters,” *Surf. Interfaces*, vol. 21, no. 100694, p. 100694, 2020.

[33] G. Dennler, H.-J. Prall, R. Koeppe, M. Egginger, R. Autengruber, and N. S. Sariciftci, “Enhanced spectral coverage in tandem organic solar cells,” *Appl. Phys. Lett.*, vol. 89, no. 7, p. 073502, 2006.

[34] M. Riede, D. Spoltore, and K. Leo, “Organic solar cells - the path to commercial success,” *Adv. Energy Mater.*, vol. 11, no. 1, p. 2002653, 2021.

[35] A. Rivaton, A. Tournebize, J. Gaume, P.-O. Bussière, J.-L. Gardette, and S. Therias, “Photostability of organic materials used in polymer solar cells: Photostability of polymer solar cells,” *Polym. Int.*, vol. 63, no. 8, pp. 1335–1345, 2014.

[36] H. Zhang, A. Borgschulte, F. A. Castro, R. Crockett, A. C. Gerecke, O. Deniz, J. Heier, S. Jenatsch, F. Nüesch, C. Sanchez-Sanchez, and A. Zoladek-Lemanczyk, “Photochemical transformations in fullerene and molybdenum oxide affect the stability of bilayer organic solar cells,” *Adv. Energy Mater.*, vol. 5, no. 2, p. 1400734, 2015.

[37] Q. Burlingame, X. Tong, J. Hankett, M. Slootsky, Z. Chen, and S. R. Forrest, “Photochemical origins of burn-in degradation in small molecular weight organic photovoltaic cells,” *Energy Environ. Sci.*, vol. 8, no. 3, pp. 1005–1010, 2015.

[38] B. Conings, S. Bertho, K. Vandewal, A. Senes, J. D’Haen, J. Manca, and R. A. Janssen, “Modeling the temperature-induced degradation kinetics of the short circuit current in organic bulk heterojunction solar cells,” *Appl. Phys. Lett.*, vol. 96, no. 16, p. 163301, 2010.

[39] A. Kojima, K. Teshima, Y. Shirai, and T. Miyasaka, “Organometal halide perovskites as visible-light sensitizers for photovoltaic cells,” *J. Am. Chem. Soc.*, vol. 131, no. 17, pp. 6050–6051, 2009.

[40] J.-H. Im, C.-R. Lee, J.-W. Lee, S.-W. Park, and N.-G. Park, “6.5% efficient perovskite quantum-dot-sensitized solar cell,” *Nanoscale*, vol. 3, no. 10, pp. 4088–4093, 2011.

[41] H. S. Kim, C. R. Lee, J. H. Im, K. B. Lee, T. Moehl, A. Marchioro, S. J. Moon, R. Humphry-Baker, J. H. Yum, J. E. Moser, and M. Grätzel, “Lead iodide perovskite sensitized all-solid-state submicron thin film mesoscopic solar cell with efficiency exceeding 9%,” *Sci. Rep.*, vol. 2, no. 1, p. 591, 2012.

[42] J. Burschka, N. Pellet, S. J. Moon, R. Humphry-Baker, P. Gao, M. K. Nazeeruddin, and M. Grätzel, “Sequential deposition as a route to high-performance perovskite-sensitized solar cells,” *Nature*, vol. 499, no. 7458, pp. 316–319, 2013.

[43] “Best research-cell efficiency chart,” *Nrel.gov*. [Online]. Available: https://www.nrel.gov/pv/cell-efficiency.html. [Accessed: 03-Nov-2021].

[44] I. Mora-Seró, “How do perovskite solar cells work?” *Joule*, vol. 2, no. 4, pp. 585–587, 2018.

[45] M. H. Ann, J. Kim, M. Kim, G. Alosaimi, D. Kim, N. Y. Ha, J. Seidel, N. Park, J. S. Yun, and J. H. Kim, “Device design rules and operation principles of high-power perovskite solar cells for indoor applications,” *Nano Energy*, vol. 68, no. 104321, p. 104321, 2020.

[46] A. Marchioro, J. Teuscher, D. Friedrich, M. Kunst, R. Van De Krol, T. Moehl, M. Grätzel, and J. E. Moser, “Unravelling the mechanism of photoinduced charge transfer

processes in lead iodide perovskite solar cells," *Nat. Photonics*, vol. 8, no. 3, pp. 250–255, 2014.

[47] W. E. I. Sha, X. Ren, L. Chen, and W. C. H. Choy, "The efficiency limit of $CH_3NH_3PbI_3$ perovskite solar cells," *Appl. Phys. Lett.*, vol. 106, no. 22, p. 221104, 2015.

[48] G. Grancini, A. R. S. Kandada, J. M. Frost, A. J. Barker, M. De Bastiani, M. Gandini, S. Marras, G. Lanzani, A. Walsh, and A. Petrozza, "Role of microstructure in the electron-hole interaction of hybrid lead halide perovskites," *Nat. Photonics*, vol. 9, no. 10, pp. 695–701, 2015.

[49] N.-G. Park, "Perovskite solar cells: an emerging photovoltaic technology," *Mater. Today (Kidlington)*, vol. 18, no. 2, pp. 65–72, 2015.

[50] B. Luo, F. Li, K. Xu, Y. Guo, Y. Liu, Z. Xia, and J. Z. Zhang, "B-site doped lead Halide perovskites: Synthesis, band engineering, photophysics, and light emission applications," *J. Mater. Chem. C Mater. Opt. Electron. Devices*, vol. 7, no. 10, pp. 2781–2808, 2019.

[51] P. Roy, N. Kumar Sinha, S. Tiwari, and A. Khare, "A review on perovskite solar cells: Evolution of architecture, fabrication techniques, commercialization issues and status," *Sol. Energy*, vol. 198, pp. 665–688, 2020.

[52] T. Webb, S. J. Sweeney, and W. Zhang, "Device architecture engineering: Progress toward next-generation perovskite solar cells," *Adv. Funct. Mater.*, vol. 31, no. 35, p. 2103121, 2021.

[53] B. Salhi, Y. S. Wudil, M. K. Hossain, A. Al-Ahmed, and F. A. Al-Sulaiman, “Review of recent developments and persistent challenges in the stability of perovskite solar cells,” *Renew. Sustain. Energy Rev.*, vol. 90, pp. 210–222, 2018.

[54] F. Zhang, D. Bi, N. Pellet, C. Xiao, Z. Li, J. J. Berry, S. M Zakeeruddin, K. Zhu, and M. Grätzel, “Suppressing defects through the synergistic effect of a Lewis base and a Lewis acid for highly efficient and stable perovskite solar cells,” *Energy Environ. Sci.*, vol. 11, no. 12, pp. 3480–3490, 2018.

[55] Y.-H. Kye, C.-J. Yu, U.-G. Jong, Y. Chen, and A. Walsh, “Critical role of water in defect aggregation and chemical degradation of perovskite solar cells,” *J. Phys. Chem. Lett.*, vol. 9, no. 9, pp. 2196–2201, 2018.

[56] W. Tan, A. R. Bowring, A. C. Meng, M. D. McGehee, and P. C. McIntyre, “Thermal stability of mixed cation metal Halide perovskites in air,” *ACS Appl. Mater. Interfaces*, vol. 10, no. 6, pp. 5485–5491, 2018.

[57] Y. Ouyang, Y. Li, P. Zhu, Q. Li, Y. Gao, J. Tong, L. Shi, Q. Zhou, C. Ling, Q. Chen, and Z. Deng, “Photo-oxidative degradation of methylammonium lead iodide perovskite: mechanism and protection,” *J. Mater. Chem. A Mater. Energy Sustain.*, vol. 7, no. 5, pp. 2275–2282, 2019.

[58] R. Wang, M. Mujahid, Y. Duan, Z.-K. Wang, J. Xue, and Y. Yang, “A review of perovskites solar cell stability,” *Adv. Funct. Mater.*, vol. 29, no. 47, p. 1808843, 2019.

[59] H. Chen, “Interface and composition engineering towards stable and efficient organic-inorganic perovskite solar cells,” Friedrich-Alexander-Universität Erlangen-Nürnberg (FAU), Bavaria, Germany, 2018.

[60] F. Corsini and G. Griffini, “Recent progress in encapsulation strategies to enhance the stability of organometal halide perovskite solar cells,” *J. Phys. Energy*, vol. 2, no. 3, p. 031002, 2020.

[61] A. Uddin, M. Upama, H. Yi, and L. Duan, “Encapsulation of organic and perovskite solar cells: A review,” *Coatings*, vol. 9, no. 2, p. 65, 2019.

[62] M. Kim, A. Alfano, G. Perotto, M. Serri, N. Dengo, A. Mezzetti, S. Gross, M. Prato, M. Salerno, A. Rizzo, and R. Sorrentino, “Moisture resistance in perovskite solar cells attributed to a water-splitting layer,” *Commun Mater*, vol. 2, no. 1, 2021.

[63] C. Peike, I. Hädrich, K. A. Weiß, I. Dürr, and F. Ise, “Overview of PV module encapsulation materials.”

[64] E. Ramasamy, V. Karthikeyan, K. Rameshkumar, and G. Veerappan, “Glass-to-glass encapsulation with ultraviolet light curable epoxy edge sealing for stable perovskite solar cells,” *Mater. Lett.*, vol. 250, pp. 51–54, 2019.

[65] A. Asadpoordarvish, A. Sandström, S. Tang, J. Granström, and L. Edman, “Encapsulating light-emitting electrochemical cells for improved performance,” *Appl. Phys. Lett.*, vol. 100, no. 19, p. 193508, 2012.

[66] B.-J. Kim, J. H. Jang, J. Kim, K. S. Oh, E. Y. Choi, and N. Park, “Efficiency and stability enhancement of organic-inorganic perovskite solar cells through micropatterned Norland Optical Adhesive and polyethylene terephthalate encapsulation,” *Mater. Today Commun.*, vol. 20, no. 100537, p. 100537, 2019.

[67] G. S. Han, H. S. Jung, and N.-G. Park, “Recent cutting-edge strategies for flexible perovskite solar cells toward commercialization,” *Chem. Commun. (Camb.)*, 2021.

[68] C. A. Aranda, L. Caliò, and M. Salado, “Toward commercialization of stable devices: An overview on encapsulation of hybrid organic-inorganic perovskite solar cells,” *Crystals (Basel)*, vol. 11, no. 5, p. 519, 2021.

[69] F. Matteocci, L. Cinà, E. Lamanna, S. Cacovich, G. Divitini, P. A. Midgley, C. Ducati, and A. Di Carlo, “Encapsulation for long-term stability enhancement of perovskite solar cells,” *Nano Energy*, vol. 30, pp. 162–172, 2016.

[70] L. Shi, T. L. Young, J. Kim, Y. Sheng, L. Wang, Y. Chen, Z. Feng, M. J. Keevers, X. Hao, P. J. Verlinden, and M. A. Green, “Accelerated lifetime testing of organic-inorganic perovskite solar cells encapsulated by polyisobutylene,” *ACS Appl. Mater. Interfaces*, vol. 9, no. 30, pp. 25073–25081, 2017.

[71] J. Li, R. Xia, W. Qi, X. Zhou, J. Cheng, Y. Chen, G. Hou, Y. Ding, Y. Li, Y. Zhao, and X. Zhang, “Encapsulation of perovskite solar cells for enhanced stability: Structures, materials, and characterization,” *J. Power Sources*, vol. 485, no. 229313, p. 229313, 2021.

[72] R. Cheacharoen, N. Rolston, D. Harwood, K. A. Bush, R. H. Dauskardt, and M. D. McGehee, “Design and understanding of encapsulated perovskite solar cells to withstand temperature cycling,” *Energy Environ. Sci.*, vol. 11, no. 1, pp. 144–150, 2018.

[73] D. Barreiro-Argüelles, G. Ramos-Ortiz, J.-L. Maldonado, E. Pérez-Gutiérrez, D. Romero-Borja, and A. Álvarez-Fernández, “PTB7:PC71BM-based solar cells fabricated with the eutectic alloy field’s metal as an alternative cathode and the influence of an electron extraction layer,” *IEEE J. Photovolt.*, vol. 7, no. 1, pp. 191–198, 2017.

[74] D. Barreiro-Argüelles, G. Ramos-Ortiz, J. L. Maldonado, E. Pérez-Gutiérrez, D. Romero-Borja, M. A. Meneses-Nava, and J. C. Nolasco, "Stability study in organic solar cells based on PTB7:PC71BM and the scaling effect of the active layer," *Sol. Energy*, vol. 163, pp. 510–518, 2018.

[75] D. Romero-Borja, J. L. Maldonado, O. Barbosa-García, M. Rodríguez, A. de León, S. Fernández, and E. Pérez-Gutiérrez, "Organic solar cells based on graphene derivatives and eutectic alloys vacuum-free deposited as top electrodes," *Carbon N. Y.*, vol. 134, pp. 301–309, 2018.

[76] Y. Wu, Y. Fang, Z. Fan, and C. Liu, "Accurate morphology characterization using atomic force microscopy via vertical drift correction and illusory slope elimination," *Microsc. Microanal.*, pp. 1–9, 2021.

[77] S. S. van Bavel, M. Bärenklau, G. de With, H. Hoppe, and J. Loos, "P3HT/PCBM bulk heterojunction solar cells: Impact of blend composition and 3D morphology on device performance," *Adv. Funct. Mater.*, vol. 20, no. 9, pp. 1458–1463, 2010.

[78] G. Zhang, X. K. Chen, J. Xiao, P. C. Chow, M. Ren, G. Kupgan, X. Jiao, C. C. Chan, X. Du, R. Xia, and Z. Chen, "Delocalization of exciton and electron wavefunction in non-fullerene acceptor molecules enables efficient organic solar cells," *Nat. Commun.*, vol. 11, no. 1, p. 3943, 2020.

[79] M. Rangel, M. Güizado-Rodríguez, J. L. Maldonado, R. Olayo-Valles, V. Barba, and J. U. Reveles, "Eco-friendly synthesis of regioregular poly(3-hexylthiophene) by direct arylation polymerization: Analysis of the properties that determine its performance in BHJ solar cells," *Polymer (Guildf.)*, vol. 193, no. 122348, p. 122348, 2020.

[80] M. Shaban, M. Benghanem, A. Almohammedi, and M. Rabia, “Optimization of the active layer P3HT:PCBM for organic solar cell,” *Coatings*, vol. 11, no. 7, p. 863, 2021.

[81] W. Cao and J. Xue, “Recent progress in organic photovoltaics: device architecture and optical design,” *Energy Environ. Sci.*, vol. 7, no. 7, p. 2123, 2014.

[82] M.-H. Jao, H.-C. Liao, and W.-F. Su, “Achieving a high fill factor for organic solar cells,” *J. Mater. Chem. A Mater. Energy Sustain.*, vol. 4, no. 16, pp. 5784–5801, 2016.

[83] D. Hu, Q. Yang, H. Chen, F. Wobben, V. M. Le Corre, R. Singh, T. Liu, R. Ma, H. Tang, L. J. A. Koster, and T. Duan, “15.34% efficiency all-small-molecule organic solar cells with an improved fill factor enabled by a fullerene additive,” *Energy Environ. Sci.*, vol. 13, no. 7, pp. 2134–2141, 2020.

[84] S. B. Sapkota, A. Spies, B. Zimmermann, I. Dürr, and U. Würfel, “Promising long-term stability of encapsulated ITO-free bulk-heterojunction organic solar cells under different aging conditions,” *Sol. Energy Mater. Sol. Cells*, vol. 130, pp. 144–150, 2014.

[85] A. Krishna, H. Zhang, Z. Zhou, T. Gallet, M. Dankl, O. Ouellette, F. T. Eickemeyer, F. Fu, S. Sanchez, M. Mensi, and S. M. Zakeeruddin, “Nanoscale interfacial engineering enables highly stable and efficient perovskite photovoltaics,” *Energy Environ. Sci.*, vol. 14, no. 10, pp. 5552–5562, 2021.

[86] I. Mesquita, L. Andrade, and A. Mendes, “Effect of relative humidity during the preparation of perovskite solar cells: Performance and stability,” *Sol. Energy*, vol. 199, pp. 474–483, 2020.

[87] Y. H. Soo, S. A. Ng, Y. H. Wong, and C. Y. Ng, "Thermal stability enhancement of perovskite MAPbI3 film at high temperature (150 °C) by PMMA encapsulation," *J. Mater. Sci.: Mater. Electron.*, vol. 32, no. 11, pp. 14885–14900, 2021.

[88] E. Pérez-Gutiérrez, M. J. Percino, P. Santos, M. Cerón, P. Ceballos, D. M. Montoya, O./ Barbosa-García, and S. Thamotharan, "Compositional study of mixed halide perovskite films $CH_3NH_3Pb(I1\text{-}Br)_3$ and $CH_3NH_3Pb(I1\text{-}Cl)_3$ prepared by close space sublimation," *Mater. Today Commun.*, vol. 25, no. 101384, p. 101384, 2020.

[89] E. Pérez-Gutiérrez, M. J. Percino, D. M. Montoya, D. Solis-Ibarra, M. Cerón, and O. Barbosa-García, "Control of the morphology and crystallinity of a PbI_2 layer for large-area perovskite films prepared by close space sublimation," *ACS Appl. Energy Mater.*, vol. 1, no. 8, pp. 3843–3849, 2018.

[90] M. Wong-Stringer, O. S. Game, J. A. Smith, T. J. Routledge, B. A. Alqurashy, B. G. Freestone, A. J. Parnell, N. Vaenas, V. Kumar, M. O. Alawad, And A. Iraqi, "High-performance multilayer encapsulation for perovskite photovoltaics," *Adv. Energy Mater.*, vol. 8, no. 24, p. 1801234, 2018.

[91] *Norlandprod.com*. [Online]. Available: https://www.norlandprod.com/adhchart.html. [Accessed: 03-Nov-2021].

[92] Y. Jiang, L. Qiu, E. J. Juarez-Perez, L. K. Ono, Z. Hu, Z. Liu, L. Meng, Q. Wang, and Y. Qi, "Reduction of lead leakage from damaged lead halide perovskite solar modules using self-healing polymer-based encapsulation," *Nat. Energy*, vol. 4, no. 7, pp. 585–593, 2019.